Monthly Notices
of the
ROYAL ASTRONOMICAL SOCIETY

MNRAS **502,** 3885–3910 (2021)
Advance Access publication 2021 February 9

doi:10.1093/mnras/stab263

The clustering of critical points in the evolving cosmic web

J. Shim [1], S. Codis,[2,3]★ C. Pichon [1,2,3] D. Pogosyan [1,4] and C. Cadiou [5]

[1]*Korea Institute for Advanced Study, 85 Hoegiro, Dongdaemun-gu, 02455 Seoul, Republic of Korea*
[2]*Institut d'Astrophysique de Paris, UMR 7095, CNRS and Sorbonne Université, 98 bis Boulevard Arago, F-75014 Paris, France*
[3]*IPhT, DRF-INP, UMR 3680, CEA, Orme des Merisiers Bat 774, F-91191 Gif-sur-Yvette, France*
[4]*Department of Physics, University of Alberta, 11322-89 Avenue, Edmonton, AB T6G 2G7, Canada*
[5]*Department of Physics and Astronomy, University College London, London WC1E 6BT, UK*

Accepted 2021 January 26. Received 2021 January 25; in original form 2020 October 30

ABSTRACT

Focusing on both small separations and baryonic acoustic oscillation scales, the cosmic evolution of the clustering properties of peak, void, wall, and filament-type critical points is measured using two-point correlation functions in ΛCDM dark matter simulations as a function of their relative rarity. A qualitative comparison to the corresponding theory for Gaussian random fields allows us to understand the following observed features: (i) the appearance of an exclusion zone at small separation, whose size depends both on rarity and signature (i.e. the number of negative eigenvalues) of the critical points involved; (ii) the amplification of the baryonic acoustic oscillation bump with rarity and its reversal for cross-correlations involving negatively biased critical points; (iii) the orientation-dependent small-separation divergence of the cross-correlations of peaks and filaments (respectively voids and walls) that reflects the relative loci of such points in the filament's (respectively wall's) eigenframe. The (cross-) correlations involving the most non-linear critical points (peaks, voids) display significant variation with redshift, while those involving less non-linear critical points seem mostly insensitive to redshift evolution, which should prove advantageous to model. The ratios of distances to the maxima of the peak-to-wall and peak-to-void over that of the peak-to-filament cross-correlation are $\sim\sqrt{2}$ and $\sim\sqrt{3}$, respectively, which could be interpreted as the cosmic crystal being on average close to a cubic lattice. The insensitivity to redshift evolution suggests that the absolute and relative clustering of critical points could become a topologically robust alternative to standard clustering techniques when analysing upcoming surveys such as *Euclid* or Large Synoptic Survey Telescope (LSST).

Key words: methods: analytical – methods: data analysis – methods: statistical – large-scale structure of Universe.

1 INTRODUCTION

The clustering properties of the cluster and galaxy distribution in extragalactic surveys have been historically a major source of information for cosmology (Peebles 1970, 1981; Press & Schechter 1974; Bahcall & Soneira 1983; Kaiser 1986, 1991; Voit 2005; Estrada, Sefusatti & Frieman 2009; Veropalumbo et al. 2016; Marulli et al. 2018). The *N*-point functions of the galaxies themselves have received most attention (Hawkins et al. 2003; Gaztañaga et al. 2005; Kulkarni et al. 2007; Gil-Marín et al. 2015). But more recently, with larger upcoming spectroscopic or photometric surveys,[1] the specific clustering of special features in the density field like peaks (Peacock & Heavens 1985; Regos & Szalay 1995; Matsubara & Codis 2020) and voids has drawn significant renewed interest (Padilla, Ceccarelli & Lambas 2005; Chan, Hamaus & Desjacques 2014; Clampitt, Jain & Sánchez 2016; Liang et al. 2016; Lares et al. 2017; Liu et al. 2017). The cross-correlations between density minima and galaxies also have been investigated (Paz et al. 2013; Hamaus et al. 2014; Clampitt et al. 2016; Liang et al. 2016). Whereas peaks are regions of collapsing overdensity, voids are underdense regions, which make them sensitive to physics beyond the standard model while evolving in a quasi-linear regime (Sheth & van de Weygaert 2004; Hamaus et al. 2015; Stopyra, Peiris & Pontzen 2021). They offer a unique environment to test alternative theories of gravity or dark energy (Clampitt, Cai & Li 2013; Spolyar, Sahlén & Silk 2013; Barreira et al. 2015; Cai, Padilla & Li 2015; Voivodic et al. 2017; Baker et al. 2018). Massive neutrinos are also known to impact the properties of voids, be it their bias (Schuster et al. 2019), their size distribution (Massara et al. 2015; Banerjee & Dalal 2016), or their two-point correlation functions (2pCFs; Kreisch et al. 2019).

According to the standard theory of structure formation, the critical points of the density field (or cosmic fields in general) are typically the sites where the most over- and underdense non-linear structures form. For example, massive galaxy clusters are known to be anchored to high peaks of the underlying density field (Kaiser 1984; Bardeen et al. 1986; Bond et al. 1991; Ludlow & Porciani 2011). On the other hand, cosmic voids are commonly detected as large and underdense volumes surrounding local density minima, although the internal structure and dynamics of identified voids may differ depending on the void identification algorithm. In line with the association of the physical structures with extreme points of the matter density field, one can analogously relate large-scale filamentary (Fard, Taamoli & Baghram 2019) and sheet-like structures to the particular sets of, for example filament- and wall-type saddle

★ E-mail: codis@iap.fr

[1]*Euclid*, Large Synoptic Survey Telescope (LSST), *WFIRST*, *SPHEREx*, WEAVE, Maunakea Spectroscopic Explorer (MSE), Subaru Prime Focus Spectrograph (PFS), to name a few.

points, of the matter density field. Consequently, the main skeletal structure of the cosmic web (Bond, Kofman & Pogosyan 1996) can be possibly traced and examined with the special points and lines connecting these points (Sousbie et al. 2008; Pogosyan et al. 2009; Sousbie, Colombi & Pichon 2009; Gay, Pichon & Pogosyan 2012; Codis, Pogosyan & Pichon 2018). Thus, investigating the clustering properties of these special points can provide clues for understanding the spatial organization of large-scale structures of the cosmic web.

In this paper, our main objective is to extend those investigation towards the cosmic evolution of the full set of components of the cosmic web focusing on autocorrelation functions of filaments and walls on the one hand, and cross-correlation of voids, peaks, walls, and filaments on the other, with critical points of the density field serving as a proxy for the corresponding cosmic web components. Indeed, this subset of special points within the density field has remarkable topological properties that make them more robust to systematics, while their Lagrangian two-point statistics can be computed from first principle, making explicit their (initial) dependency on the underlying cosmological parameters.

Our focus is on the baryonic acoustic oscillation (BAO) scale, since it is one of the most prominent signatures of two-point functions (McDonald & Eisenstein 2007; Crocce & Scoccimarro 2008; Desjacques 2008) that has now been clearly identified in surveys (Percival et al. 2010; Beutler et al. 2011; Blake et al. 2011a; Font-Ribera et al. 2014) and used to infer cosmological parameters. We also aim to study the redshift evolution of the exclusion zone at smaller scale (Baldauf et al. 2016; Desjacques, Jeong & Schmidt 2018), together with the shape of the 2pCFs near their maximum. This should prove to be a useful dark energy probe, since e.g. 2pCFs of walls inform us about the characteristic size of voids whose redshift evolution provides information on cosmological parameters (Li, Zhao & Koyama 2012; Cai et al. 2015; Hamaus et al. 2015, 2016, 2017; Pisani et al. 2015; Verza et al. 2019). We will also study the angular dependence of the cross-correlations involving saddle points as measured in their eigenframe, i.e. to say the oriented stacking of extrema (voids or peaks) in the frame of a saddle point understood as the middle of a filament. We will also investigate the redshift evolution of those cross-correlation functions together with their dependence with the rarity of the critical points.

Section 2 presents the simulations and the estimators used to identify critical points and compute their correlations. Section 3 presents number density counts and clustering measurements in the simulation's snapshots. Section 4 identifies the pseudo-cubic lattice structure of the cosmic web, while Section 5 concludes.

Appendix A presents theoretical predictions for Gaussian random fields, while Appendix B discusses briefly the divergence at small separation of the cross-correlations between peaks and filaments (respectively wall and voids).

For clarity, we have systematically presented in the main text all auto- and cross-correlations measured in the simulation as a function of abundance and redshift, and postponed the theoretical correlations for Gaussian random fields to the Appendices, to which we refer on a case-by-case basis in the main text. Tables 3–6 present a summary of the typical scales and amplitudes characterizing these correlations.

2 METHOD

Let us first describe the simulations we used to compute the position of critical points before presenting the corresponding clustering estimator.

2.1 Simulations

We have run 532 vanilla Λ cold dark matter (ΛCDM) simulations in a 500 h^{-1} Mpc box using the cosmological parameters $\Omega_{\rm b} = 0.04$, $\Omega_{\rm m} = 0.24$, $\Omega_\Lambda = 0.76$, $h = 0.70$, $\sigma_8 = 0.8$, $n_{\rm s} = 1$. Each simulation follows 256^3 particles down to redshift zero using GADGET2 (Springel, Yoshida & White 2001). At each snapshot, the density field is sampled on a 256^3 grid smoothed with a Gaussian filter over $R_{\rm G} = 6\,h^{-1}$ Mpc. We identified the range of redshifts not impacted by transients in the simulation ($z \leq 4$) by computing ratios of the expectation of higher order cumulants of the field (commonly referred to as reduced cumulants) and comparing to expectation from tree-order perturbation theory. We binned the snapshots in the range of $0 \leq z < 4$ into five subsamples, three with $\Delta z = 1$ for $4 < z \leq 1$, $0.5 \leq z < 1$, and $0 \leq z < 0.5$. The corresponding root mean square (rms) fluctuation of the density field averaged over the snapshots in each redshift bin increases with time from $\sigma = 0.18$ ($3 \leq z < 4$) to $\sigma = 0.56$ ($0 \leq z < 0.5$) and allows us to probe the mildly non-linear regime of structure formation that is the sweet spot for extracting cosmological information thanks to higher order statistics beyond the weakly non-linear regime that can be captured from first principle calculations. Note that this set of simulations was also used in Cadiou et al. (2020) to study critical events corresponding to the mergers of critical points.

2.2 Estimators for critical statistics

2.2.1 *Critical points definition*

The critical points of a field are points where the gradient vanishes (Milnor 1963; Bardeen et al. 1986; Arnold 2006). There exist different types of critical points that are classified by the sign of the eigenvalues of the Hessian matrix (the matrix of the second derivatives of the field) at that point. Based on the typical shape of the isosurfaces in their neighbourhood, we typically call the four types of critical points in the 3D cosmic density field as peaks, filament-type saddle points, wall-type saddle points, and voids. According to the sign of their eigenvalues, one can categorize these points into extrema having eigenvalues with identical sign (peaks with signature $---$ and voids $+++$) and saddle points having one eigenvalue with a different sign (filament-type saddles with signature $--+$ and wall-type saddles with signature $-++$). We will also label the signature of a critical point by the number of negative eigenvalues, differing by one from three for the peaks to zero for the voids. Note that the terms peak, filament, wall, and void represent critical points of the density field, but not necessarily physical large-scale structures. Critical points can be associated with physical structures of the same type, however their typical sizes will depend on the smoothing scale of the density field. Objects of different size and masses are present at a fixed redshift slice, and smoothing of the density acts as a resolution effect. In this paper, we use 6 h^{-1} Mpc Gaussian smoothing, which corresponds to $\approx 10^{15}$ $\mathrm{M}_\odot$ average density region. Only the highest 5 per cent of all density peaks at this resolution represent the virialized galaxy clusters at $z = 0$ while the rest are still in the process of the collapse. Accordingly, this smoothing erases small-scale structures in the void interiors, focusing on large voids.

2.2.2 *Finding critical points*

In order to identify critical points in a smoothed simulated field, a local quadratic estimation is used. The detection relies on a second-order Taylor expansion of the density field. About a critical point,

Table 1. Total number of peaks ($\mathcal{P}$), filaments ($\mathcal{F}$), walls ($\mathcal{W}$), and voids ($\mathcal{V}$) in different redshift bins.

	$\mathcal{P}$	$\mathcal{F}$	$\mathcal{W}$	$\mathcal{V}$
$0 \leq z < 0.5$	3690	10 542	10 098	3209
$0.5 \leq z < 1$	3693	10 712	10 377	3324
$1 \leq z < 2$	3690	10 857	10 631	3434
$2 \leq z < 3$	3689	10 999	10 872	3542
$3 \leq z < 4$	3713	11 138	11 064	3620

this yields

$$\boldsymbol{x} - \boldsymbol{x}_{\rm c} \approx (\nabla\nabla\rho)^{-1}\,\nabla\rho, \tag{1}$$

where $\boldsymbol{x}_{\rm c}$ is the position of the critical point and ρ is the density field. The detection algorithm[2] then works as follows. (a) For each cell in the grid, compute the gradient and Hessian of the density field; (b) solve equation (1) and discard all solutions found at a distance greater than 1 pixel ($\max_{i=1,\dots3}(|\boldsymbol{x}_i - \boldsymbol{x}_{\rm c}|) < 1$ pixel); (c) flag each cell containing a critical point; and (d) finally, loop over flagged cells that contain multiple critical points of the same kind, retaining for each only the critical point closest to the centre of the cell (see also Gay et al. 2012, appendix G). The numbers of identified peaks, filaments, walls, and voids are tabulated in Table 1.

2.2.3 *Computing clustering properties*

To measure their clustering properties, we count the pairs of critical points with rarity above or below a certain threshold. The rarity of the critical point is defined as

$$\nu \equiv \delta/\sigma, \tag{2}$$

where δ is the overdensity contrast of the smoothed density field,

$$\delta \equiv \rho/\bar{\rho} - 1, \tag{3}$$

and σ is the rms fluctuation of the field,

$$\sigma^2 \equiv \left\langle \delta^2 \right\rangle. \tag{4}$$

For peak and filament (respectively void and wall) critical points, we extract points with rarity higher (respectively lower) than a given threshold. In this paper, we fix this threshold as the rarity for each type of critical points, $\nu_{\rm type,\,c}$, yielding the same relative abundances (e.g. 5, 10, 15, 20 per cent) defined by the ratios

$$\frac{N_{\rm type}(\nu \geq \nu_{\rm type,c})}{N_{\rm type}}, \tag{5}$$

for peaks and filaments, and

$$\frac{N_{\rm type}(\nu \leq \nu_{\rm type,c})}{N_{\rm type}}, \tag{6}$$

for voids and walls, in each redshift bin.

Our purpose is to single out the redshift evolution of the clustering properties by sampling the population that represents the same abundance for a given type of critical points. This somewhat ad hoc choice allows us to limit the number of configurations we investigate, and imposes non-intersecting ranges of rarities (ν) for peak and void on the one hand, and walls and filaments on the other. This choice was driven by symmetry, but has consequences: for instance, the chosen wall saddle points do not represent well what one would identify as say, the great Sloan Digital Sky Survey (SDSS) wall, which is an overdense feature of the large-scale structure (LSS). The lack of overlap in rarities also impacts exclusion zones, see Appendix B for more details. Note, however, that all the machinery developed in this paper could easily be applied to any choice of abundances for the critical points.

Using critical points extracted by applying these particular rarity thresholds, we measure the correlation functions with the estimator adopted in Cadiou et al. (2020), simply given by a Davis–Peebles estimator (Davis & Peebles 1983)

$$1 + \xi_{ij}(r) = \frac{\langle C_i C_j \rangle}{\sqrt{\langle C_i R_j \rangle \langle C_j R_i \rangle}} \sqrt{\frac{N_{R_i} N_{R_j}}{N_{C_i} N_{C_j}}}, \tag{7}$$

where C_i denotes a particular catalogue of critical points $i \in \{\mathcal{P}, \mathcal{F}, \mathcal{W}, \mathcal{V}\}$ and R_i is a corresponding random catalogue with randomly distributed points following a uniform probability distribution in the same volume. Here $\langle XY \rangle$ represents number counts of the pairs between X and Y whose separation is r. The sample size, N_{R_i}, of the random catalogue for extrema (respectively saddles) is a factor of 100 (respectively 200) larger than the correspondent size of our simulated data sets, N_{C_i}. Note that periodic boundary conditions are taken into account when computing distances.

3 COUNTS AND CLUSTERING MEASUREMENTS

Let us describe the results of our measurements in ΛCDM simulations. The corresponding theory for Gaussian random fields is presented in Appendix A. We will focus first on the total (Section 3.1) and differential number counts of critical points (Section 3.2) as a function of rarity, then present their autocorrelations (Section 3.3) before studying their cross-correlations (Section 3.4). In particular, we will focus on the angular dependence of the cross-correlations involving saddle points as measured in their eigenframe (Section 3.4.3) to understand how the geometry of the cosmic web impacts clustering.

3.1 Total number of critical points

As quoted in Table 1, we identified more peaks than voids. As expected, this deviates from Gaussian predictions for which those two numbers are equal (Bardeen et al. 1986). Indeed, the non-linear evolution tends to break the symmetry between underdense and overdense regions and in particular between peaks and voids. The number difference between them is shown to be larger at lower redshifts. This is also true for filaments and walls that should appear in the same proportion in the Gaussian regime and should be approximately three[3] times more abundant than peaks and voids. Gay et al. (2012) showed that the first non-linear correction has the same amplitude for all kinds of critical points, with the same sign for peaks and filaments and the opposite sign for walls and voids. Hence, the total number of extrema (voids and peaks together) is preserved at first non-Gaussian order, similarly for the total number of saddles and therefore also their ratio. Interestingly, this property pervades as the measured number ratio of saddles over extrema remains nearly constant (close to 3) in our simulations throughout the redshift range investigated. Note that for sufficiently large volumes, we expect the

[2]The code is available at PY-EXTREMA.

[3]For Gaussian random field, the ratio between the numbers of filaments and peaks (or walls and voids) is exactly $(29\sqrt{15} + 18\sqrt{10})/(29\sqrt{15} - 18\sqrt{10}) \approx 3.05$.

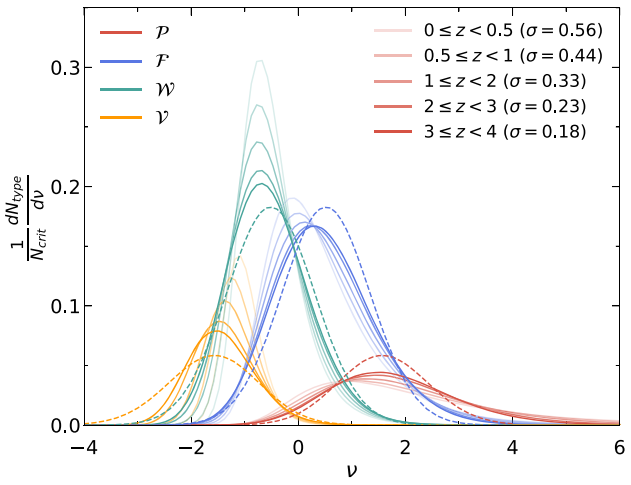

Figure 1. Relative number counts of critical points ($\mathcal{P}$: peaks; $\mathcal{F}$: filaments; $\mathcal{W}$: walls; and $\mathcal{V}$: voids) as functions of their rarity in different redshift bins and the corresponding $\sigma(z)$ of the field, as labelled. The number counts in the Gaussian limit (dashed) are also displayed. At all redshifts, they show distinctive non-Gaussian asymmetry that becomes more pronounced at late time (as predicted by perturbation theory). These counts will allow us to define thresholds containing a given percentage of all critical points of a given kind, when looking at auto- and cross-correlations between critical points. Note how strikingly the position of the maximum of the wall counts varies so little with redshift. The maximum amplitude of void and wall counts continuously increase from the Gaussian limit to the lowest redshift, while peak counts decrease. Interestingly, the maximum of the filament counts first decreases from the Gaussian prediction and then increases at later times. In most cases, the counts become narrower as they evolve, except for peaks.

ratio between the number of peaks and walls over filaments and voids to be very close to one throughout the redshift evolution, which is indeed the case here. This is because the topology of the box hence the genus that is the alternating sum of critical points should be preserved. Note finally that the numbers of different critical points decrease with time, although the ratio of extrema over saddles remains constant. Given the level of non-linearity at the redshifts investigated here, it is required to perform higher than first-order perturbation theory predictions to properly capture and explain the decreasing trend of the number of critical points.

3.2 One-point function of critical points

Let us now study the distribution of rarity of the measured critical points. Fig. 1 shows the relative number counts of critical points as functions of rarity. The number counts of a particular type is normalized by that of all critical points in each snapshot. These measurements underpin the relations between rarity thresholds and abundances given in Table 2. In the Gaussian limit, the distributions of peaks and voids (respectively filaments and walls) are symmetric to each other about $\nu = 0$ (Bardeen et al. 1986). However, as the density field becomes non-linear and non-Gaussian, such symmetries break down (see for instance Gay et al. 2012). At low redshift, we observe that the rarity distributions of critical points become narrower and have higher maximum amplitude except for peak critical points. The relative number counts for the peak and filament critical points clearly show a positively skewed rarity distribution driven by gravitational clustering. In particular, their relative number count at the highest end slightly increases with decreasing redshift as overdense regions become denser with time. This behaviour is similar in essence to the so-called Edgeworth expansion incorporating probabilists' Hermite polynomials H_n and cumulant ratios S_n,

$$P(\nu) = \exp(-\nu^2/2)\,[1 + \sigma\, S_3 H_3(\nu) + \cdots]\,, \tag{8}$$

of the density field (not restricted to critical points) whose mildly non-Gaussian probability density function (PDF) is well captured by perturbative techniques (Bernardeau & Kofman 1995), and even more so when a large-deviation principle is used to include consistently more non-linearities (Bernardeau, Pichon & Codis 2014). Similar techniques can be used in the context of critical points, as was for instance derived for arbitrary non-Gaussianities in Gay et al. (2012). Here, cumulants involving not only the density field – as is the case for the skewness S_3 – but also its first and second derivatives appear. However, note that the prediction for the differential counts is not analytical (even at Gaussian order) but can be evaluated numerically.

Qualitatively, the behaviour of the redshift evolution in Fig. 1 seems consistent with e.g. fig. 6 in Gay et al. (2012) (which in turn was shown to agree with perturbation theory predictions), and allows us to probe the range of non-linearity $\sigma > 0.18$ that starts where Gay et al. (2012) analysis ends, $\sigma < 0.2$. In particular, the evolution from the initial Gaussian conditions to the highest redshift range having similar σ shows a very good agreement. For example, the position of the maximum of the distribution displays almost no evolution for peaks and voids but shifts to the left for walls and filaments. The maximum becomes higher compared to the Gaussian prediction for voids and walls, whereas it decays for filaments and peaks. Interestingly, the trend of the maximum moving towards rarities of smaller magnitude persists to the lowest redshift bins for all critical points except walls. For walls, the position of the maximum is almost stationary at $z < 3$ after having moved to the left from the initial maximum position in Gaussian limit. On the other hand, the height evolution of the maximum is monotonic for all types except for filaments, for which the evolution happens in two successive stages. As seen in Gay et al. (2012) (and tentatively in the very high redshift bins here), the maximum of the relative number count first goes down and then we find it to increase again when non-Gaussianities continue to rise.

From the differential number counts of critical points, we can identify the thresholds that will be used to compute correlation functions. Table 2 provides the mean thresholds $\nu_{\mathrm{type,\,c}}$ for all types of critical points and various abundances in the five redshift bins we consider. As expected, the threshold increases for rarer peaks as the field becomes more non-Gaussian with redshift. Notable is a relative stability with redshift of the rarity threshold for filament-type saddle points at fixed abundance except for the rarest abundance threshold for which an increase with non-linearity is observed similar to peaks. We also note the trend for underdense voids and walls opposite to peaks, for which the rarity threshold decreases in magnitude as the field evolves, probably as a result of the positive skewness that dominates in the first stage of structure formation.

3.3 Autocorrelation of critical points

Having characterized the one-point statistics of critical points, let us now turn to their autocorrelations.

3.3.1 Rarity dependence of the autocorrelations: Fig. 2

Let us first study the autocorrelation of critical points at low redshift for different rarities, before studying their redshift evolution. Fig. 2 shows the autocorrelations of critical points with different

Table 2. Threshold used on the rarities of critical points ($\nu_{\rm type,\,c}$) so as to keep a fixed abundance (given by the N per cent rarest objects) at various redshifts. These values are redshift dependent because of the development of non-Gaussianities in the relative number counts (see Fig. 1). The last column also displays the predictions for Gaussian random fields.

Type	Abundance (per cent)	$0 \leq z < 0.5$ ($\sigma = 0.56$)	$0.5 \leq z < 1$ ($\sigma = 0.44$)	$1 \leq z < 2$ ($\sigma = 0.33$)	$2 \leq z < 3$ ($\sigma = 0.23$)	$3 \leq z < 4$ ($\sigma = 0.18$)	$z \to \infty$ ($\sigma \to 0$)
$\mathcal{P}$	20	3.43	3.28	3.08	2.85	2.73	2.30
	15	3.98	3.73	3.45	3.15	2.99	2.46
	10	4.74	4.36	3.95	3.55	3.33	2.67
	5	6.09	5.42	4.77	4.18	3.87	2.98
$\mathcal{F}$	20	1.13	1.19	1.23	1.25	1.25	1.21
	15	1.39	1.44	1.46	1.46	1.45	1.37
	10	1.76	1.79	1.78	1.74	1.71	1.57
	5	2.40	2.36	2.29	2.19	2.12	1.87
$\mathcal{W}$	20	− 0.90	− 0.97	− 1.04	− 1.10	− 1.14	− 1.21
	15	− 0.96	− 1.05	− 1.13	− 1.21	− 1.26	− 1.37
	10	− 1.03	− 1.14	− 1.24	− 1.35	− 1.41	− 1.57
	5	− 1.12	− 1.26	− 1.39	− 1.53	− 1.62	− 1.87
$\mathcal{V}$	20	− 1.24	− 1.41	− 1.60	− 1.79	− 1.91	− 2.30
	15	− 1.27	− 1.46	− 1.66	− 1.88	− 2.01	− 2.46
	10	− 1.31	− 1.51	− 1.74	− 1.98	− 2.13	− 2.67
	5	− 1.37	− 1.59	− 1.85	− 2.13	− 2.30	− 2.98

abundances between 5 per cent and 20 per cent and for low redshifts, $0 \leq z < 0.5$. We split the plots for separations between 0 and 60 h^{-1} Mpc (left-hand panels) and BAO scales (right-hand panels). Let us recall that, for peaks and filaments (respectively voids and walls), we extract critical points above (respectively below) the rarity yielding a particular abundance (see Table 2).

The shape of the autocorrelation functions always follows the same qualitative pattern: at small separations, they are negative corresponding to a region of anticlustering ($\xi < 0$), then increase and get positive reaching a maximum at separations $\approx 3R_{\rm G}$ for peaks and voids and $\approx 2.2R_{\rm G}$ for filaments and walls, before gradually decreasing towards zero in the large-separation regime where bias expansions can be performed (Desjacques et al. 2018). This behaviour has been investigated in details for Gaussian peaks in many works including in 1D (Baldauf et al. 2016) and in 3D (Baldauf et al. 2020) where in particular the typical size of the anticlustering region and its scaling with the peak heights difference $\propto (\Delta\nu)^{1/3}$ were derived. Note that if one naively associates Gaussian full width at half-maximum (FWHM) $= 2.35\,R_{\rm G}$ with a size of peak footprint, finding the correlation maximum at 1.3–1.4 FWHM shows that rare peaks tend to come in rather tightly packed clusters.

Let us now describe our findings for the dependence of the autocorrelations with the rarity of the objects, based on Fig. 2. At a general level, as shown in the left-hand panels, the main trends found for all types of critical points with increasing rarity are threefold: enhanced clustering (i.e. larger overprobability $1 + \xi$), a maximum for the 2pCF occurring at a radius that is only weakly decreasing, and a narrower anticlustering region.

In more detail, at large separations $r \gtrsim 5\,R_{\rm G} \approx 30\ h^{-1}$ Mpc, the increase of the autocorrelation amplitude for rarer critical points, implying a stronger clustering, can be explained with a simple linear bias[4] of critical points relative to the dark matter correlation function $\xi_{0,\,0}$, $\xi_{\mathcal{P}\mathcal{P}} \sim b_{10}^2(\nu)\xi_{0,0}/\sigma_0^2 \sim \nu^2\xi_{0,0}/\sigma_0^2$ that reflects a known effect of stronger clustering of more biased tracers (Kaiser 1984; Desjacques 2008; Uhlemann et al. 2017; Desjacques et al. 2018). This not only holds for the positively biased tracers such as peaks and filaments but also for the negative cases of void and wall points. Interestingly, the trend in void-point autocorrelations is analogous to that in autocorrelations of cosmic voids. Indeed, similar to rarer void points being more clustered, the clustering of cosmic voids is also enhanced for larger voids (Padilla et al. 2005; Clampitt et al. 2016; Lares et al. 2017). This may imply that a lower density minimum is typically associated with a larger void.

One can go beyond the simple linear bias and derive a peak bias expansion assuming all correlation functions are small compared to their zero lag (see also Appendix A). We refer the reader to the review Desjacques et al. (2018) for more details. Predictions up to order three (Matsubara & Codis 2020) have been obtained for Gaussian peaks but the convergence of these expansions is slow and cannot capture the small and intermediate scales including the maximum of the 2pCF and even more so their exclusion zone for which a full numerical integration is required. They are none the less very useful to understand the large separation region including BAO scales as was extensively studied by notably Desjacques (2008), Desjacques et al. (2010), and Baldauf & Desjacques (2017).

In the intermediate regime of the 2pCF the main feature is the maximum of the autocorrelation. While its height continues to reflect the larger bias and more pronounced clustering of the rarer objects, we also point out that the position of the maximum correlation shifts toward lower separations as rarity increases (at least for peaks and voids), an approximately 10 per cent effect between 5 per cent and 20 per cent abundant peaks at $0 \leq z < 0.5$. Let us also note that the height of the maximum of the autocorrelations for filaments and walls is about a factor of 2 higher than those for peaks and voids for a given abundance. This may be related to different curvature conditions, via the second derivatives of the density field, between extrema and saddles. Note also that the radius of maximum correlation is typically smaller for saddles than for extrema. Quantities at special locations including the maximum at intermediate separation and inflection point at large scale of the correlation functions for various abundances are listed in Table 3. We calculate the standard deviation of the mean quantities at the lowest redshift snapshot in each redshift bin as a proxy to the typical scatter of the mean quantities in each redshift

[4] $b_{10}(\nu) \sim \nu/\sigma_0$ in the high ν limit, see Appendix A.

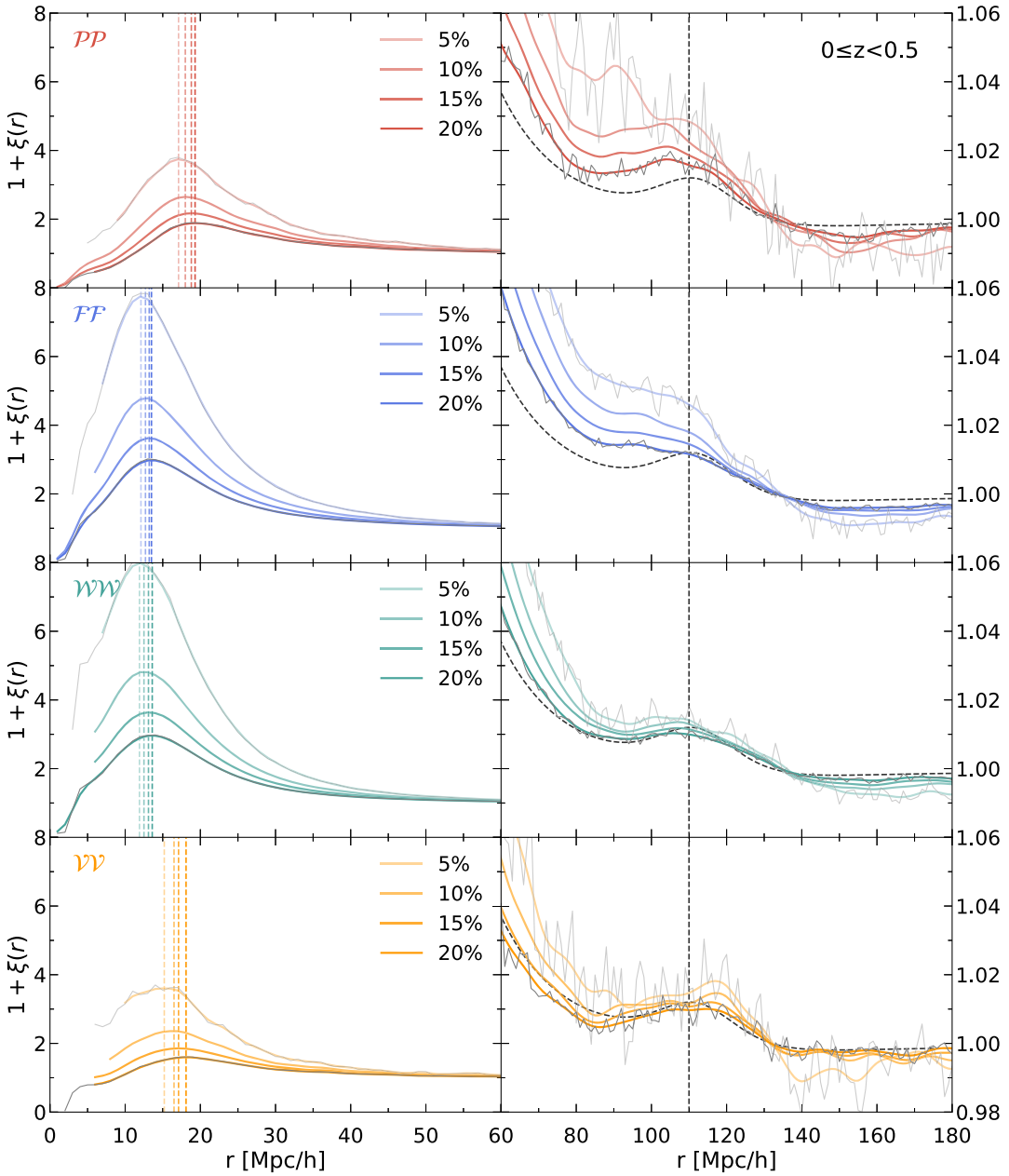

Figure 2. Autocorrelations of critical points with different abundances for separations between 0 and 60 h^{-1} Mpc (left) and BAO scales (right) for $0 \leq z < 0.5$. $\mathcal{PP}$ (peak–peak), $\mathcal{FF}$ (filament–filament), $\mathcal{WW}$ (wall–wall), and $\mathcal{VV}$ (void–void) correlations are shown in panels from top to bottom. Smoothed versions (non-grey) of the measurements and unsmoothed measurements (grey) for abundances between 5 per cent and 20 per cent are presented. The linear matter correlation function at the corresponding median redshift (multiplied by 8 which is close to the square of the bias factor for $\nu_{\rm peak} \geq 2.5$ for peak critical points; Matsubara & Codis 2020) is also displayed on the right-hand panels with a dashed line. The vertical lines mark respectively the position of the maximum of the autocorrelations (left) and the BAO peak position of the linear matter correlation (right). These positions are found as the local maximum using cubic–spline interpolation. Note that for $\mathcal{FF}$ and $\mathcal{WW}$ they follow closely each other. For rarer critical points, the maxima of the correlations move to the left and become higher. At late time, the BAO positions are not very well defined regardless of the abundance in most cases. Finally, note that the inflection point at $\sim$133 h^{-1} Mpc corresponds to zero correlation for all cases.

bin. Indeed, since measurements in consecutive snapshots are correlated, measuring errors in the full bin would likely underestimate them.

The small shift of the maximum of the 2pCF towards the left with rarer critical points can be explained with rarity difference ($\Delta\nu$) that is usually smaller in rarer critical point samples. Indeed, the extent of the anticlustering region decreases with decreasing rarity difference (Baldauf et al. 2016) and hence the position of the maximum correlation moves to a smaller radius. For Gaussian random fields with the same power spectrum, the mean rarity difference can be computed and yields $\overline{\Delta\nu} = \{0.43,\ 0.40,\ 0.37,\ 0.33\}$ for abundances 20 per cent, 15 per cent, 10 per cent, and 5 per cent, respectively. If the shift of the maximum scales like $\Delta\nu^{1/3}$, as derived by Baldauf et al. (2020), then we expect a shift of 0 per cent, 2 per cent, 5 per cent, and 8 per cent of $r_{\rm max}$ with respect to the 20 per cent abundance case. If the redshift evolution is small (as will indeed

Table 3. Position and height of the maximum and the location of the inflection point in auto- and cross-correlations as a function of rarity for the lowest redshift bin, $0 \leq z < 0.5$. The errors are the standard deviations of the mean obtained from the resampled realizations at $z = 0$ using bootstrapping.

Type	Abundance (per cent)	$r_{\rm max}$ (h^{-1} Mpc)	$h_{\rm max}$	$r_{\rm inf}$ (h^{-1} Mpc)
$\mathcal{PP}$	20	19.3 ± 0.30	1.9 ± 0.01	132.7 ± 1.8
	15	18.8 ± 0.30	2.2 ± 0.02	131.9 ± 2.1
	10	18.0 ± 0.55	2.7 ± 0.03	135.7 ± 2.4
	5	17.1 ± 0.48	3.7 ± 0.07	133.7 ± 3.9
$\mathcal{FF}$	20	13.5 ± 0.08	3.0 ± 0.01	134.3 ± 1.5
	15	13.2 ± 0.11	3.6 ± 0.01	133.6 ± 1.5
	10	12.7 ± 0.15	4.8 ± 0.02	134.4 ± 1.7
	5	12.1 ± 0.14	7.8 ± 0.06	133.3 ± 1.6
$\mathcal{WW}$	20	13.6 ± 0.12	3.0 ± 0.01	136.0 ± 1.2
	15	13.1 ± 0.14	3.6 ± 0.01	134.3 ± 1.3
	10	12.5 ± 0.14	4.8 ± 0.03	134.5 ± 1.6
	5	11.9 ± 0.17	8.0 ± 0.07	134.5 ± 3.0
$\mathcal{VV}$	20	18.1 ± 0.30	1.6 ± 0.01	132.3 ± 1.6
	15	17.1 ± 0.76	1.9 ± 0.02	131.5 ± 1.2
	10	16.5 ± 1.12	2.4 ± 0.03	132.0 ± 2.2
	5	15.2 ± 0.96	3.6 ± 0.10	131.8 ± 1.9
$\mathcal{PF}$	20	13.6 ± 0.05	4.9 ± 0.01	133.2 ± 1.1
	15	13.7 ± 0.05	6.1 ± 0.02	133.5 ± 1.1
	10	13.9 ± 0.05	8.2 ± 0.03	134.5 ± 1.3
	5	13.9 ± 0.06	13.5 ± 0.08	132.9 ± 1.7
$\mathcal{WV}$	20	14.6 ± 0.06	3.8 ± 0.01	132.2 ± 2.4
	15	14.7 ± 0.07	4.5 ± 0.02	132.7 ± 2.2
	10	14.8 ± 0.08	5.8 ± 0.03	133.6 ± 2.9
	5	15.0 ± 0.09	8.8 ± 0.06	132.3 ± 3.1

be shown in Section 3.3.2), then those numbers can be compared to the relative shifts measured in the simulation as reported in Table 3 namely $\{0 \pm 2$ per cent, 3 ± 2 per cent, 7 ± 3 per cent, 11 ± 2 per cent$\}$ and seem perfectly consistent.

Getting to even smaller scales, all critical point autocorrelation functions seem to exhibit a zone of negative correlations, as was found before for peaks (Baldauf et al. 2016; Codis et al. 2018). From theoretical considerations, the limit $\xi(0) = -1$ is expected, though the resolution effects of our measurements do not allow to probe the immediate vicinity of the origin. The suppression of the probability of finding other critical points next to the first one happens because of constraints on curvature and height in the smoothed correlated density field. For instance, it is very unlikely to find two peaks infinitely close to each other unless the peaks have the exact same height (Baldauf et al. 2016). One can notice that the crossing of the Poisson case $\xi = 0$ seems to shift closer to the origin for larger rarity (extrapolating our measurements in the low-separation regime).

Overall, the three main features at small separation are consistent with the prediction for Gaussian random fields (see Fig. A2 in Appendix A) where we find similar rarity dependencies. In particular, as in the measurements, the Gaussian prediction also shows that filament correlations have amplitudes approximately twice as large as for peaks or that positions of the correlation maxima are somewhat closer to the origin for rarer points, in agreement with the estimate from Baldauf et al. (2020) as explained above. It is notable how well the rarity dependencies of the autocorrelations of the critical points in the relatively non-linear regime ($\sigma \approx 0.6$) are already encoded in the initial perturbations. The evolution of autocorrelations of critical points thus preserves the initial clustering properties, supporting the 'cosmic web' paradigm of Bond et al. (1996).

Let us now focus on the right-hand panels of Fig. 2 that show the autocorrelations at very large separations where correlations exhibit the BAO effect. To qualitatively describe how the large-scale features of the clustering of critical points differ from that of the dark matter, we also compute the (unsmoothed) linear dark matter correlation function by adopting the transfer functions in Eisenstein & Hu (1998).[5] We multiply the linear correlation by a factor of 8 so that it has a similar amplitude to the measured correlations of the 20 per cent rarest peak critical points. This factor can be qualitatively interpreted as the square of the large-scale bias, and reflects that the correlation is enhanced compared to the linear prediction (Kaiser 1984). Our choice of bias factor for the 20 per cent rarest peaks (with $\nu_{\rm peak} > 3.5$, see Table 2) is qualitatively consistent with the result obtained in Matsubara & Codis (2020), in which their bias factor is approximately 2.6 for peaks with $\nu_{\rm peak} > 2.5$, using a perturbative approach in the large-separation limit.

In general, all autocorrelations (except for filaments) decrease from $r \approx 20$ to $80\ h^{-1}$ Mpc. Then, they gently increase at around $100 \leq r < 120\ h^{-1}$ Mpc showing BAO-like features before dropping again at larger separation. However, the exact position of the BAO bumps is not robustly defined for all abundances: further simulations will be required to make a more quantitative comparison because the correlation function is too noisy at late time. As expected for biased tracers in general, the BAO wiggles are found to be enhanced compared to the dark matter case, an effect that persists despite the smoothing and the non-linear gravitational evolution that are known to reduce the sharpness of the BAOs. Around the BAO peak, we also find that peak and filament autocorrelations vary more with abundance than voids and walls, which might be due to very overdense regions being more prone to non-linear effects including large-scale velocity flows, that also tend to shift the BAO peak to smaller scales. Interestingly, correlation is larger for rarer points below $\approx 133\ h^{-1}$ Mpc, but it is more anticorrelated at larger radii for all types of critical points. At roughly $r \approx 133\ h^{-1}$ Mpc, the correlation goes through zero through an inflection point (corresponding to $\xi(r_{\rm inf}) = 0$ and where correlations for different abundances almost coincide) for all abundances, a feature that is also seen in the linear matter correlation. It is remarkable that most correlations go through this inflection point at the same scale (see Table 3). It is surprisingly consistent with a multiplicative linear bias model at that scale, see Appendix A and would be interesting to study further as a possible robust cosmological probe (less sensitive to non-linearities). This situation seems similar to the so-called linear point (Anselmi, Starkman & Sheth 2015; O'Dwyer et al. 2020) that is the mid-point between the first dip and peak of the BAO pattern at $\sim 100\ h^{-1}$ Mpc. This point in the halo correlation function was shown to be robust against non-linear evolution, biasing effects, and redshift-space distortions and eventually can serve as a purely geometric cosmological test without the need for assuming any prior on the cosmological model or any model for the late-time galaxy correlation function evolution. Similar features seem to occur here for this secondary inflection point in the critical point 2pCFs and would therefore be worth investigating in more details in the future.

[5]The smoothing typically reduces the sharpness of the BAO feature and may slightly shift the peak position inward.

3.3.2 Redshift evolution of the autocorrelations: Fig. 3

Let us now turn to the redshift evolution of the autocorrelations of critical points in Fig. 3. For a quantitative comparison, we provide the positions and heights of the maximum and the BAO as a function of redshift in Table 4. At small and intermediate separations ($r \leq 30\,h^{-1}$ Mpc), the shape and height of the autocorrelations show little redshift evolution. In particular, the position change of the maximum correlation is at most $\Delta r \sim 0.4\,h^{-1}$ Mpc for $0 \leq z < 4$, which is small compared to the smoothing scale ($R_G = 6\,h^{-1}$ Mpc).

On BAO scales, wiggles are clearly amplified compared to the underlying dark matter field, the features appear particularly sharp for peaks and voids and at high redshift. We detect a redshift evolution of the peak and filament autocorrelations on the left-hand side of the BAO peak. In particular, the position and height of the BAO bump change non-negligibly. For these overdense critical points, the height of the bump increases at lower redshift and its location moves toward smaller scale. Also, the bumps become less pronounced as they evolve. This is again probably because the non-linear gravitational evolution of overdense regions smears out the BAO signature through pairwise motions (Desjacques 2008). On the other hand, the autocorrelations of walls and voids show very little redshift evolution, which could be a good reason for using these underdense regions as cosmological probes. Noticeably, the position and height of the BAO bump is most stable for walls at $r \approx 106$–$108\,h^{-1}$ Mpc. Since the two-point statistics of walls is almost unchanged from high to low redshift, this is in line with the findings by Gay et al. (2012) that one-point statistics of saddle critical points, specifically, can be modelled analytically down to the mildly non-linear regime.

3.4 Cross-correlation of critical points

Let us now quantify the evolution of the cross-correlations of critical points as a function of rarity and redshift.

3.4.1 Rarity dependence of cross-correlations: Figs 4 and 5

Figs 4 and 5 show the cross-correlations of six combinations of different critical points. We will first describe the left-hand panels of the figures and then discuss the right-hand panels for cross-correlations on BAO scales.

We first show in Fig. 4 the cross-correlations between overdense and underdense critical points. The main feature of these four cross-correlations is a strong exclusion zone (see left-hand panels), where the correlation function ξ is close to -1. Note that our definition of the exclusion zone is rather strict (for comparison, see Baldauf et al. 2016). The corresponding exclusion zone radius, r_{ez}, defined implicitly by $\xi(r_{ez}) = -0.99$ is displayed with dashed vertical line and given in Table 5 together with the inflection point position for different abundance. In contrast to the autocorrelations, at $r \geq r_{ez}$, the correlation functions monotonically increase toward zero without displaying any maximum. The cross-correlations being always negative implies that overdense and underdense critical points are always anticlustered at all scales. No statistically preferred distance between these pairs of critical points can be established.

The presence of the exclusion zone is always expected for the cross-correlation of critical points that signatures differ by more than one, as well as not differ at all as in the case of autocorrelations. From curvature continuity argument, only critical points with signature differing strictly by unity, namely $\mathcal{PF}$, $\mathcal{FW}$, $\mathcal{WV}$, can approach each other when smoothly deforming the field. For the rest, the curvature has to change a sign at least twice along the line between the critical points (for instance, for two peaks, the density has to go down and then up between them) that results in statistical exclusion of near pairs. However, in Fig. 4 another effect also leads to the repulsion between close pairs, which is our choice to limit the rarities of peak and filament points to the highest (positive) end, whereas voids and walls are constrained to the lowest (negative) side. This difference of allowed density values between the overdense and underdense critical points produces the exclusion zone that can be attributed to a density continuity argument (it is highly unlikely to have large variation of density over short distances) even in the case of $\mathcal{FW}$ where the curvature repulsion effect is absent. As expected, the $\mathcal{FW}$ cross-correlations show slightly smaller exclusion zone, compared to those with a larger difference of signatures ($\mathcal{FV}$ and $\mathcal{PW}$, then $\mathcal{PV}$). This is already captured in Gaussian random fields as shown in Fig. A1.

The size of the exclusion zone – meaning the volume where the probability to have both rare overdense and rare underdense critical points is suppressed – grows with rarity. This is expected since a lower abundance threshold implies that overdense and underdense critical points have an even larger difference of rarity ($\Delta\nu$) that forces them to be further apart (the correlated density field will need a larger typical distance to be able to go from one very underdense region to one very overdense). This results in the increase of the exclusion zone as abundances go to lower percentage values. Appendix B shows how the rarity constraints change the behaviour of the cross-correlations at small separation, in particular as rarity threshold varies.

As shown in the left-hand panel of Fig. 5, the cross-correlations between critical points with the same overdensity signs are fundamentally different from those in the left-hand panels of Fig. 4. First, they diverge at zero separation and exhibit neither exclusion zones nor negative correlations at small scales. Secondly, these cross-correlations have a local maximum at $r \approx 13$–$15\,h^{-1}$ Mpc, similar to the maximum in the autocorrelation functions in Fig. 2.[6] The reason for this divergent behaviour at $r \to 0$ of peak–filament and wall–void cross-correlations is that in these cases we compare two critical points that signatures differ only by one (such that there is no need to go through one or more intermediate critical point in between, as is the case when going from peak to wall through filament for instance) and that ranges of allowed density values overlap. Such critical points can come together at $r \to 0$ in merging *critical events* (Cadiou et al. 2020). Possibility to have critical events induce positive correlation and enhanced probability of a critical pair with neighbouring signatures to be within a shrinking volume of radius $r \to 0$. This argument would extend to filament–wall cross-correlation, however this case is modified by our choice of rarity thresholds that leads to non-overlapping density values for filaments and walls in all pairs, which precludes the merging critical events. Thus, this case is not included in Fig. 5, but appeared in Fig. 4 and is discussed in more details in Appendix B (see Fig. B1).

The enhanced probability of high filamentary saddles to exist near high peaks shown in peak–filament cross-correlations matches the topological properties of the cosmic web where high peaks are the

[6]Note that we have truncated the peak–filament and the wall–void correlation functions below $r < 5\,h^{-1}$ Mpc, since the diverging feature at that scale is not fully captured by our measurements given the resolution limit of the density field. It is noteworthy that a similar divergence exists at small separation in the theoretical Gaussian prediction, for which there is no numerical resolution issue, as can be seen in Fig. A3.

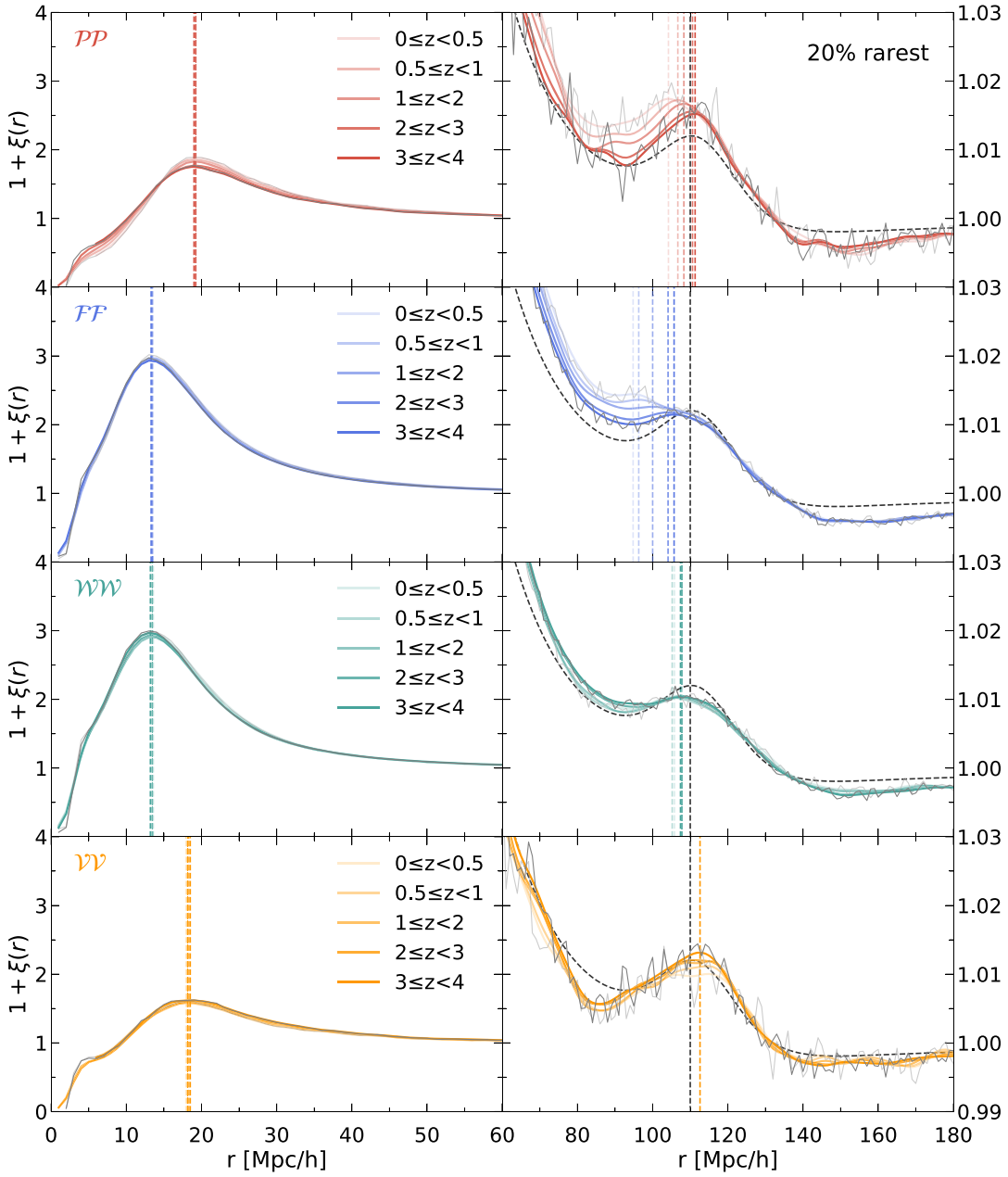

Figure 3. Autocorrelations of 20 per cent rarest critical points in different redshift bins for separations between 0 and 60 h^{-1} Mpc (left) and BAO scales (right), following the same convention for the correlation type as in Fig. 2. We present both smoothed (coloured) and unsmoothed (grey) versions of the measurements for the lowest and highest redshift bins only. The linear dark matter correlation function (dashed) at the median redshift of $0 \leq z < 0.5$ (multiplied by a factor of 8) is also presented. The vertical lines mark the positions of the maximum correlation (left) and BAOs (right) of the autocorrelation (non-black) and the linear matter correlation (black). These positions are found as the local maximum using cubic-spline interpolation. Positions for the only well-defined BAO peaks are marked at large separation. The position and height of the maximum correlation barely change with redshift. Again, $\mathcal{FF}$ and $\mathcal{WW}$ correlations follow each other, and $\mathcal{PP}$ and $\mathcal{VV}$ also are similar although $\mathcal{PP}$ case has slightly higher maximum. The BAO signal is clearly detected and amplified compared to the linear matter correlation and it is more enhanced for extrema than for saddles. Note that the BAO position is almost stationary in $\mathcal{WW}$ correlations.

nodes for filamentary branches (that eventually pass through saddles). The presence of the local maximum in their cross-correlation function points to some order in spatial distribution of saddles around the peaks, and gives a statistically preferred distance to such saddles. The typical length of filamentary bridges between two high peaks can be estimated to twice this distance. The position of the local maximum, interestingly, varies negligibly with abundance, at $r_{\rm max}$ ≈ 14 h^{-1} Mpc leading to an estimate of 28 h^{-1} Mpc for a typical bridging filament length. It is remarkably close to the 30 h^{-1} Mpc estimate given in Bond et al. (1996).

The void–wall cross-correlation is very similar to the peak–filament one (and is exactly the same for Gaussian random fields). Walls encompass the voids and define their boundary. Let us recall that by rare walls we mean the least dense ones, so our rare wall

Table 4. Positions and heights of the maximum and BAO peak in auto- and cross- correlations as a function of redshift for 20 per cent abundance. The errors are the standard deviations of the mean obtained from the resampled realizations using a bootstrap method at the lowest redshift snapshot of each redshift bin. Less well-defined BAO quantities are omitted.

Type	Redshift	$r_{\rm max}$ (h^{-1} Mpc)	$h_{\rm max}$	$r_{\rm BAO}$ (h^{-1} Mpc)	$h_{\rm BAO}$
$\mathcal{PP}$	$0 \le z < 0.5$	19.3 ± 0.30	1.88 ± 0.01	104.2 ± 2.4	1.017 ± 0.001
	$0.5 \le z < 1$	19.0 ± 0.43	1.86 ± 0.01	106.7 ± 1.8	1.017 ± 0.001
	$1 \le z < 2$	19.1 ± 0.23	1.83 ± 0.01	108.3 ± 1.2	1.017 ± 0.001
	$2 \le z < 3$	19.1 ± 0.32	1.77 ± 0.01	110.6 ± 1.9	1.016 ± 0.001
	$3 \le z < 4$	19.0 ± 0.29	1.75 ± 0.01	111.3 ± 0.9	1.016 ± 0.001
$\mathcal{FF}$	$0 \le z < 0.5$	13.5 ± 0.08	2.98 ± 0.01	94.8 ± 2.5	1.014 ± 0.001
	$0.5 \le z < 1$	13.5 ± 0.10	2.97 ± 0.01	96.3 ± 1.5	1.014 ± 0.001
	$1 \le z < 2$	13.4 ± 0.08	2.96 ± 0.01	100.0 ± 2.3	1.013 ± 0.001
	$2 \le z < 3$	13.4 ± 0.08	2.95 ± 0.01	104.1 ± 2.4	1.012 ± 0.001
	$3 \le z < 4$	13.3 ± 0.07	2.93 ± 0.01	105.7 ± 1.2	1.012 ± 0.001
$\mathcal{WW}$	$0 \le z < 0.5$	13.6 ± 0.12	2.96 ± 0.01	105.8 ± 1.7	1.010 ± 0.001
	$0.5 \le z < 1$	13.5 ± 0.11	2.94 ± 0.01	105.2 ± 1.2	1.010 ± 0.001
	$1 \le z < 2$	13.4 ± 0.10	2.91 ± 0.01	107.4 ± 1.0	1.010 ± 0.001
	$2 \le z < 3$	13.2 ± 0.12	2.93 ± 0.01	107.7 ± 1.0	1.011 ± 0.001
	$3 \le z < 4$	13.2 ± 0.08	2.97 ± 0.01	107.4 ± 2.3	1.010 ± 0.001
$\mathcal{W}$	$0 \le z < 0.5$	18.1 ± 0.30	1.60 ± 0.01	–	–
	$0.5 \le z < 1$	18.0 ± 0.30	1.58 ± 0.01	–	–
	$1 \le z < 2$	18.2 ± 0.50	1.58 ± 0.01	–	–
	$2 \le z < 3$	18.3 ± 0.54	1.59 ± 0.01	–	–
	$3 \le z < 4$	18.5 ± 0.90	1.62 ± 0.01	112.6 ± 5.8	1.013 ± 0.001
$\mathcal{PF}$	$0 \le z < 0.5$	13.6 ± 0.05	4.93 ± 0.01	96.4 ± 3.3	1.015 ± 0.001
	$0.5 \le z < 1$	13.6 ± 0.05	4.76 ± 0.01	96.9 ± 5.2	1.014 ± 0.001
	$1 \le z < 2$	13.7 ± 0.05	4.58 ± 0.01	106.2 ± 4.7	1.013 ± 0.001
	$2 \le z < 3$	13.8 ± 0.05	4.43 ± 0.01	108.0 ± 2.4	1.013 ± 0.001
	$3 \le z < 4$	13.7 ± 0.04	4.34 ± 0.01	108.1 ± 1.2	1.013 ± 0.001
$\mathcal{W}\mathcal{F}$	$0 \le z < 0.5$	14.6 ± 0.06	3.78 ± 0.01	105.9 ± 3.0	1.010 ± 0.001
	$0.5 \le z < 1$	14.5 ± 0.06	3.82 ± 0.01	106.0 ± 3.9	1.010 ± 0.001
	$1 \le z < 2$	14.4 ± 0.06	3.84 ± 0.01	109.8 ± 3.1	1.011 ± 0.001
	$2 \le z < 3$	14.2 ± 0.06	3.92 ± 0.01	110.2 ± 2.5	1.011 ± 0.001
	$3 \le z < 4$	14.1 ± 0.05	4.01 ± 0.01	109.1 ± 1.3	1.011 ± 0.001

saddles are the points through which voids percolate first. According to our measurements, the preferred distance to them designated by the position of the local correlation maximum is $r_{\rm max} \approx 15\ h^{-1}$ Mpc. It can potentially be interpreted as the typical largest radius of a sphere centred at the void extremum that can be inscribed into the void boundaries. Recalling that the halo mass-scale corresponding to a $6\ h^{-1}$ Mpc Gaussian filtering is roughly $10^{15}\ {\rm M}_{\odot}$, it is interesting to find that this preferred distance is close to the typical radius of cosmic voids at $z = 0$ (Ruiz et al. 2015), whose halo analogue has a mass equal to $10^{15}\ h^{-1}\ {\rm M}_{\odot}$ (Shim et al. 2020).

We also note that the correlation amplitude shows a clear dependence on the critical point abundances, increasing with rarity. This points towards an even stronger statistical regularity in the relative spatial distribution of the very rare peaks and filaments, and voids and walls.

At the mildly non-linear stage ($0 \le z < 0.5$) exhibited in Fig. 5, we find a higher maximum for peak–filament cross-correlations than for the wall–void case, indicating that the clustering of the overdense pairs is stronger than that of their underdense counterpart with the same abundance. This is an effect of the non-linear evolution, since in the linear Gaussian limit $\mathcal{PF}$ and $\mathcal{WW}$ pairs are exactly symmetric. We shall look at this non-linear evolution in more detail in the following section.

When compared to the Gaussian case in Fig. A1, the measured cross-correlations in the left-hand panels of Figs 4 and 5 are qualitatively consistent with the predictions. Cross-correlations between peaks and underdense points (i.e. walls or voids) are increasing functions of the radius, going from $\xi = -1$ to 0. The exclusion zone is clearly visible until radius up to $\sim 3R_{\rm G}$ ($\sim 18\ h^{-1}$ Mpc). The size of the exclusion zone (slightly) increases similarly to the measurements as $r_{{\rm ez},\mathcal{PV}} > r_{{\rm ez},\mathcal{PW}} \approx r_{{\rm ez},\mathcal{FV}} > r_{{\rm ez},\mathcal{FW}}$, where $r_{{\rm ez},\mathcal{PV}}$, $r_{{\rm ez},\mathcal{PW}}$, $r_{{\rm ez},\mathcal{FV}}$, and $r_{{\rm ez},\mathcal{FW}}$ represent the radius of the exclusion zone for peak–void, peak–wall, filament–void, and filament–wall, respectively. While the existence of the exclusion zone stems from the curvature and density differences, let us emphasize again that the ordering can be explained through a geometrical argument. Indeed, one can go directly from a filament to a wall, while going from a peak to a wall (respectively from a filament to a void) requires going through a filament (respectively a wall). We therefore expect the exclusion zone of filament with walls to be less extended than that of peaks with walls and filaments with voids. With a similar argument, we expect the largest exclusion zone to be found for peak–void pairs, since going from one to the other requires going through a wall and a filament.

Let us now move to the right-hand panels of Figs 4 and 5 that focus on BAO scale. On these large scales, the acoustic features

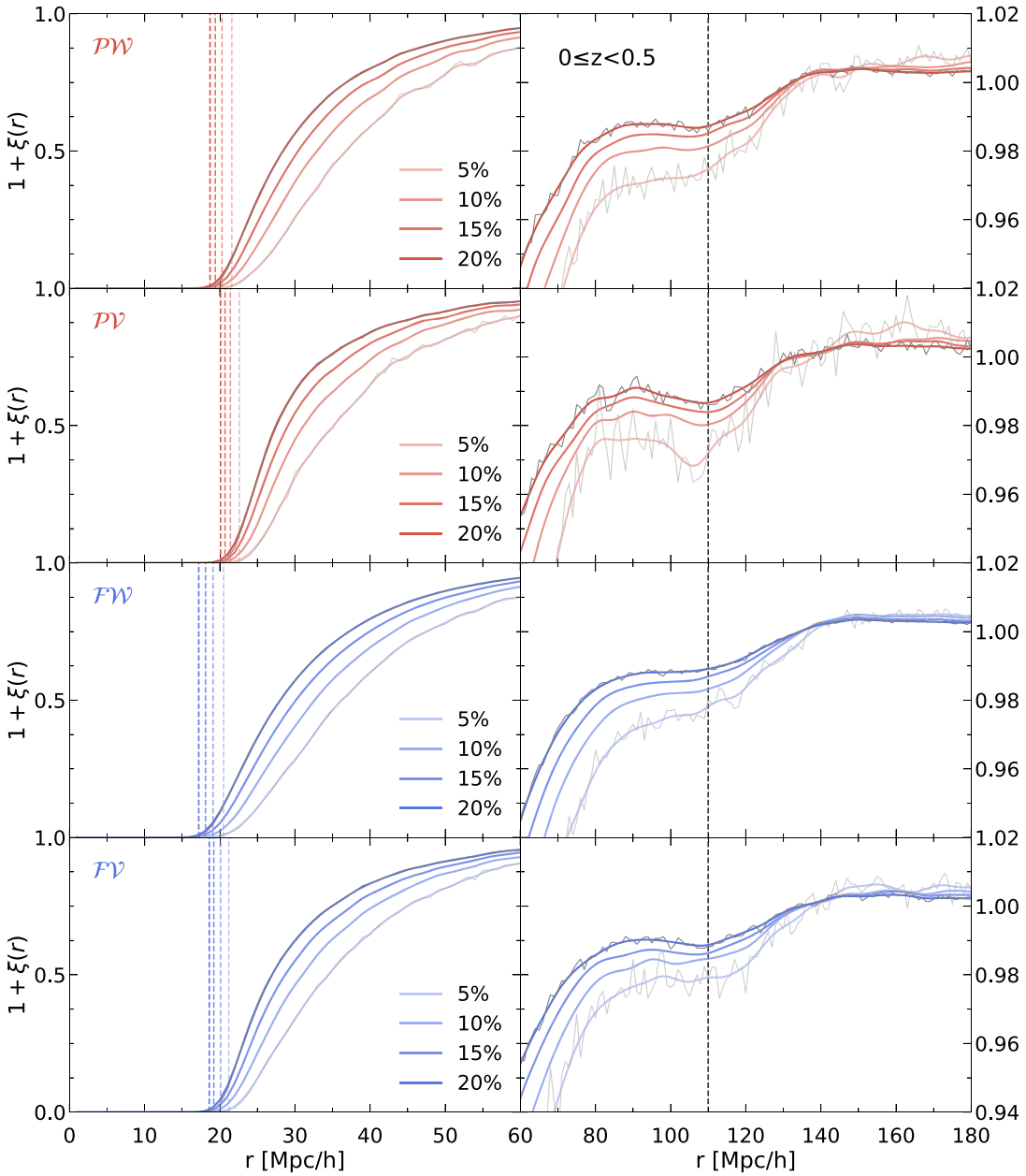

Figure 4. Cross-correlations of critical points with different abundance for separations between 0 and 60 h^{-1} Mpc (left) and BAO scales (right) and for $0 \leq z < 0.5$. $\mathcal{PW}$ (peak–wall), $\mathcal{PV}$ (peak–void), $\mathcal{FW}$ (filament–wall), and $\mathcal{FV}$ (filament–void) correlations are shown in panels from top to bottom. For these cross-correlations, the vertical lines mark the size of exclusion zone (left) and the BAO position of the linear matter correlation (right). In contrast to the autocorrelations, the exclusion zone is well defined, and its size changes with abundance (as marked by the vertical lines). Because of the curvature constraints at critical points, the exclusion zone increases with the number of eigenvalues with different sign between two critical points. Interestingly, at both small and large separation, the impact of abundance is significant. The BAO signature now corresponds to a dip in the correlation rather than a bump, which, given our choice of rarity, is mainly driven by the fact that one out of two bias factors is negative.

appear very different in the two figures although always broader than in the dark matter correlation function. For points with different density signs (Fig. 4), the BAO signature is shown as a dip in all cross-correlations, whereas it corresponds to a bump for points with the same density sign (Fig. 5) including the previous autocorrelations. The BAO dip in the right-hand panels of Fig. 4 actually represents a stronger anticlustering at the BAO scale since ξ is negative until $r \approx 133\ h^{-1}$ Mpc. This is a direct consequence of the fact that the voids and walls we consider have a negative rarity ν whose corresponding bias factor is negative (see e.g. fig. 9 of Uhlemann et al. 2017). Interestingly, the inflection points occur again at about 133 h^{-1} Mpc that is consistent with the autocorrelations (see Table 5).

As for the cross-correlations of critical points with the same density sign, the BAOs appear as a bump (as the bias factors have the same sign in this case hence their product is positive) whose position is poorly defined and noisy (right-hand panels of Fig. 5). As can be seen on these plots, we detect a stronger dependence on the abundance for the peak–filament correlations. This is consistent with the results for the autocorrelations that were showing relatively larger amplitude

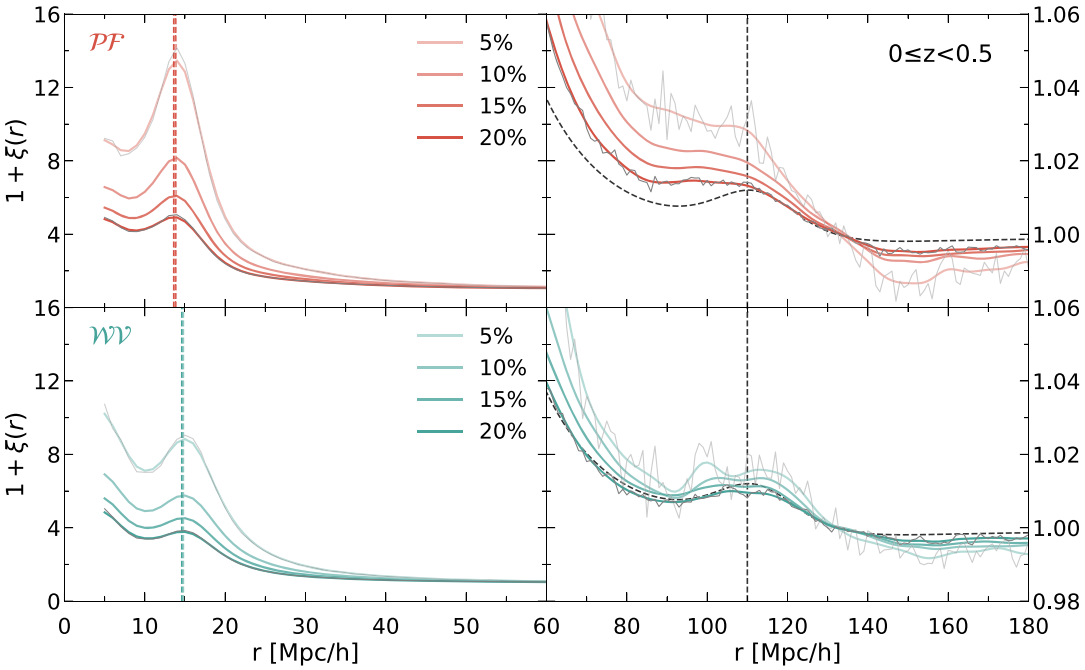

Figure 5. Same as Fig. 4, but for $\mathcal{PF}$ (peak–filament) and $\mathcal{WV}$ (wall–void) correlations in the top and bottom panels, respectively. For these cross-correlations, the vertical lines mark the positions of the maximum (left) and the BAO feature (right). We truncate the correlation function below $r < 5\ h^{-1}$ Mpc, since the pair counts at separation near the resolution scale ($\sim 2\ h^{-1}$ Mpc) are numerically suppressed. The linear dark matter correlation function (dashed) at the median redshift of $0 \leq z < 0.5$ (multiplied by a factor of 8) is also presented. Strikingly, these cross-correlations have a maximum plus a divergence-like shape at small separation, reflecting a shell-like structure in the distribution of saddles around a given extremum (see Fig. 9). In fact, the $\mathcal{PF}$ correlation of Gaussian random field also diverges at very small separation showing a head and shoulder pattern (see Fig. A3 and also fig. 4 in Codis et al. 2018). Note that the amplitude of the maximum in the left-hand panel is higher for overdense pairs, i.e. $\mathcal{PF}$. A clear abundance dependence is shown at small separation but it is less pronounced in the $\mathcal{WV}$ case at large separation. The BAO bumps shown in the cross-correlations are broader than that in the linear dark matter correlation.

Table 5. Exclusion zone radius $r_{\rm ez}$ and position of inflection point $r_{\rm inf}$ in cross-correlations as a function of rarity for the lowest redshift bin, $0 \leq z < 0.5$. The errors are the standard deviations of the mean obtained from the resampled realizations at $z = 0$ using a bootstrap method.

Type	Abundance (per cent)	$r_{\rm ez}$ (h^{-1} Mpc)	$r_{\rm inf}$ (h^{-1} Mpc)
$\mathcal{PW}$	20	18.7 ± 0.03	132.4 ± 0.9
	15	19.4 ± 0.05	132.6 ± 1.0
	10	20.3 ± 0.07	133.3 ± 1.2
	5	21.6 ± 0.11	135.2 ± 4.4
$\mathcal{PV}$	20	20.1 ± 0.05	132.3 ± 2.4
	15	20.7 ± 0.05	133.2 ± 3.9
	10	21.4 ± 0.07	134.8 ± 4.3
	5	22.6 ± 0.19	138.2 ± 3.2
$\mathcal{FW}$	20	17.2 ± 0.02	134.5 ± 1.2
	15	18.1 ± 0.04	134.7 ± 1.1
	10	19.1 ± 0.04	135.0 ± 1.2
	5	20.5 ± 0.09	137.8 ± 1.7
$\mathcal{FV}$	20	18.6 ± 0.03	134.6 ± 2.1
	15	19.2 ± 0.05	135.3 ± 2.6
	10	20.1 ± 0.06	135.7 ± 2.8
	5	21.2 ± 0.13	137.9 ± 3.4

changes on very large scales in the peak–peak and filament–filament cases than the rest of the autocorrelations. Similarly to the previous correlation functions, the location of the inflection point is robustly at $\sim 133\ h^{-1}$ Mpc (see Table 3). Note interestingly that all kinds of auto- and cross- correlations have inflection point consistently at the same scale $r_{\rm inf} \simeq 133\ h^{-1}$ Mpc.

3.4.2 *Redshift evolution of cross-correlations: Figs 6 and 7*

Let us now turn to the redshift evolution of the cross-correlation functions. In Fig. 6, we again first show peak–wall, peak–void, filament–wall, and filament–void cross-correlations but for different redshift bins. We also provide the relevant quantities for the exclusion zone and the BAO features as functions of redshift in Table 6. Similarly to the autocorrelations, the behaviour of the cross-correlations changes little with redshift. In the left-hand panels, the correlation functions for different redshift bins almost overlap with each other at small separation. In particular, the exclusion zone size remains nearly constant with redshift such that they maintain the same ordering across cosmic time: $r_{{\rm ez},\mathcal{PV}} > r_{{\rm ez},\mathcal{PW}} \approx r_{{\rm ez},\mathcal{FV}} > r_{{\rm ez},\mathcal{FW}}$.

In the right-hand panels, the BAO feature is evident in all redshift ranges. The BAO positions are stable at all redshifts and are close to that of the (unsmoothed) linear matter correlation in most cases, except the filament–wall correlation for which the wiggle gets smeared and closer to a plateau-like shape probably because those critical points are the least biased and therefore cannot overcome the effect of the smoothing thanks a curvature effect. The height at the BAO position is also redshift independent, even for the filament–wall case. These four cross-correlations are better for analysing the BAO feature than the autocorrelations since they are well defined and more stable throughout the redshift evolution.

Fig. 7 shows the redshift evolution of the peak–filament and wall–void correlations. As can be seen in the left-hand panels,

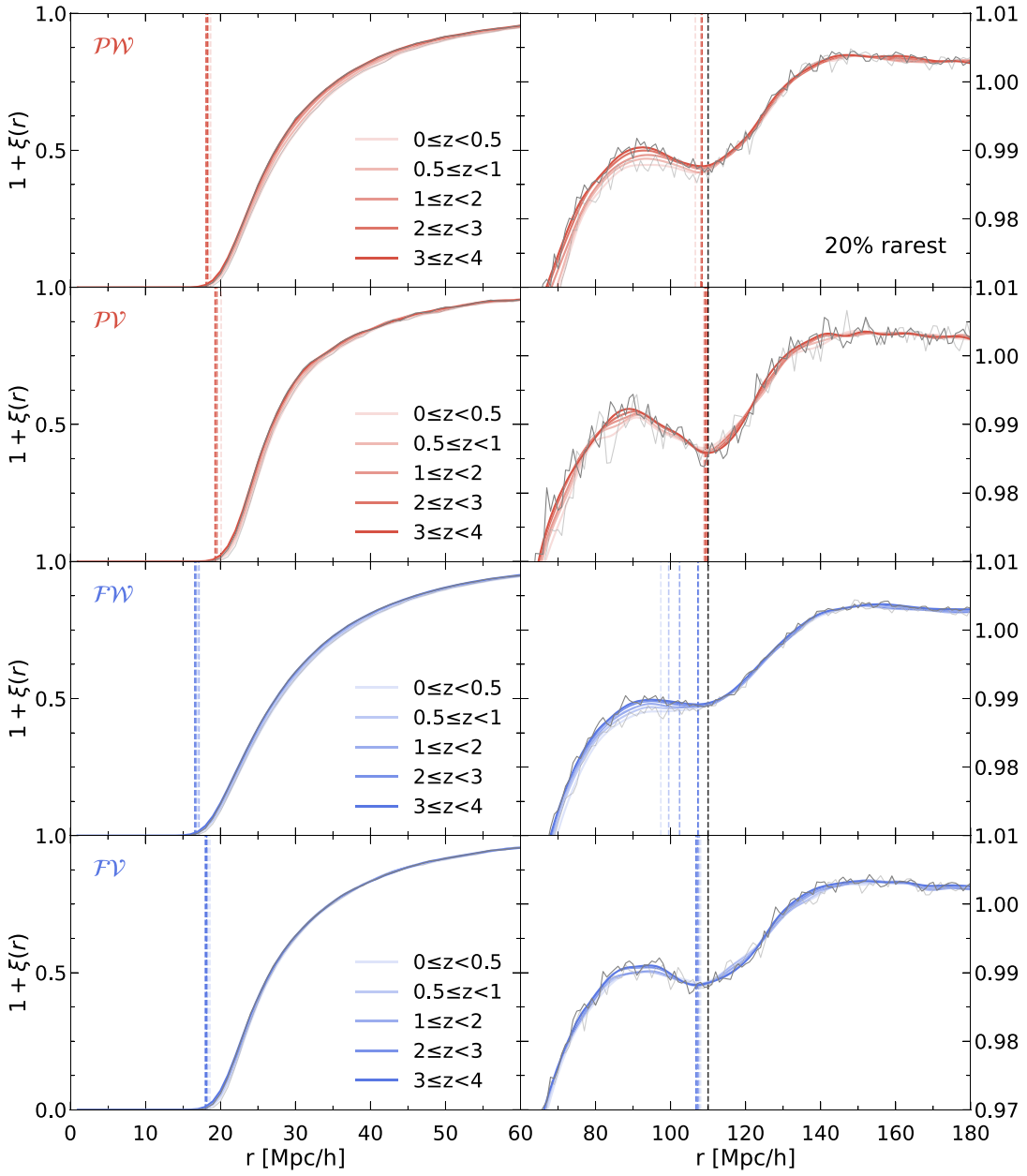

Figure 6. Following Fig. 4, the redshift evolution of the cross-correlations of the 20 per cent rarest critical points for separations between 0 and 60 h^{-1} Mpc (left) and BAO scales (right). The $\mathcal{PW}$ (peak–wall), $\mathcal{PV}$ (peak–void), $\mathcal{FW}$ (filament–wall), and $\mathcal{FV}$ (filament–void) correlations are shown from top to bottom. The vertical lines mark the exclusion zone radius (left) and the positions of BAO (right) of the cross-correlation (non-black) and the linear matter correlation (black). The size of the exclusion zone negligibly changes with time compared to Fig. 4. Interestingly, little redshift evolution of the cross-correlations is seen at large separation, although autocorrelations involving overdense critical points show a noticeable redshift variation. In most cases, the dip position of the BAO is well defined and stationary, except in the $\mathcal{FW}$ case. Note that the BAO position in the linear dark matter case is very close to that in the cross-correlations.

the region around the local maximum shows the strongest redshift evolution, in particular when compared to the diverging feature at small separation ($r < 8\ h^{-1}$ Mpc). Notably, the $\mathcal{PF}$ correlation develops a higher maximum at late time, whereas the height of the maximum is monotonically decreasing with time for the $\mathcal{WW}$ case (see Table 4). Thus the non-linear evolution of overdense pairs and underdense pairs diverges from their initially symmetric Gaussian state and their redshift evolution goes in the opposite direction: the overdense pairs become more clustered while underdense ones become slightly more uniformly distributed. Indeed, we expect peaks to become more clustered over cosmic time through their displacements as peaks are attracted towards each other, as also shown for the peak autocorrelations in Fig. 3. This effect has been for instance studied in Baldauf et al. (2020) and Regaldo-Saint Blancard et al. (2021). However, note that the redshift variation in the mildly non-linear regime probed here is weak in the $\mathcal{WW}$ cross-correlations and only somewhat more noticeable in the $\mathcal{PF}$. While the height of the maximum changes a bit, its position changes even less so with redshift. The small- and intermediate-scale behaviour of the measured $\mathcal{PF}$ correlation qualitatively agrees with the Gaussian case in Fig. A1. In particular, note that the positions of the maximum for the measurement and the Gaussian prediction are about $r \simeq$

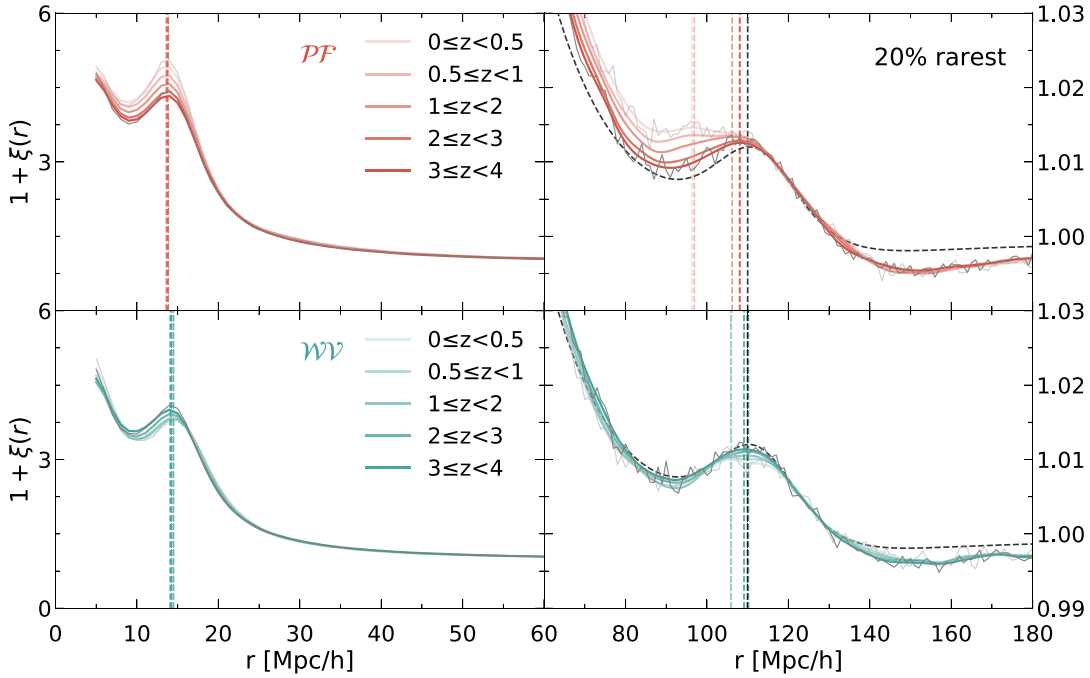

Figure 7. Same as in Fig. 6, but focusing on the redshift evolution of the cross-correlation of $\mathcal{PF}$ (peak–filament) and $\mathcal{WV}$ (wall–void) in the top and bottom panels, respectively. The linear dark matter correlation function (dashed) at the median redshift of $0 \leq z < 0.5$ (multiplied by a factor of 8) is also presented. The vertical lines mark the positions of the maximum (left) and the BAO (right) of the cross-correlation (non-black) and the linear matter correlation (black). The maximum at $\approx$15 h^{-1} Mpc barely shifts but its height changes with redshift. The height increases for $\mathcal{PF}$, whereas it decreases for $\mathcal{WV}$ with cosmic time. The BAO feature in the $\mathcal{PF}$ correlation becomes broader at lower redshift, whereas the BAO shape in the $\mathcal{WV}$ correlation negligibly changes. In general, the positions of the BAO bump for both $\mathcal{PF}$ and $\mathcal{WV}$ are stationary at all measured redshifts.

Table 6. Exclusion zone radii and positions and heights of BAO in cross-correlations as a function of redshift for 20 per cent abundance. The errors are the standard deviations of the mean obtained from the resampled realizations using a bootstrap method at the lowest redshift snapshot of each redshift bin.

Type	Redshift	$r_{\rm ez}$ (h^{-1} Mpc)	$r_{\rm BAO}$ (h^{-1} Mpc)	$h_{\rm BAO}$
$\mathcal{PW}$	$0 \leq z < 0.5$	18.7 ± 0.03	106.6 ± 3.8	0.987 ± 0.001
	$0.5 \leq z < 1$	18.4 ± 0.05	108.1 ± 1.4	0.987 ± 0.001
	$1 \leq z < 2$	18.3 ± 0.03	108.2 ± 1.0	0.987 ± 0.001
	$2 \leq z < 3$	18.2 ± 0.03	108.3 ± 1.3	0.988 ± 0.001
	$3 \leq z < 4$	18.1 ± 0.05	108.4 ± 0.9	0.988 ± 0.001
$\mathcal{PV}$	$0 \leq z < 0.5$	20.1 ± 0.05	108.8 ± 2.7	0.987 ± 0.001
	$0.5 \leq z < 1$	19.6 ± 0.05	109.1 ± 1.3	0.986 ± 0.001
	$1 \leq z < 2$	19.4 ± 0.05	109.3 ± 1.5	0.986 ± 0.001
	$2 \leq z < 3$	19.3 ± 0.05	109.5 ± 1.0	0.986 ± 0.001
	$3 \leq z < 4$	19.3 ± 0.05	109.8 ± 0.8	0.986 ± 0.001
$\mathcal{FW}$	$0 \leq z < 0.5$	17.2 ± 0.02	97.4 ± 3.3	0.988 ± 0.001
	$0.5 \leq z < 1$	17.1 ± 0.05	99.5 ± 3.8	0.989 ± 0.001
	$1 \leq z < 2$	16.8 ± 0.04	102.4 ± 3.0	0.989 ± 0.001
	$2 \leq z < 3$	16.7 ± 0.01	107.4 ± 2.7	0.989 ± 0.001
	$3 \leq z < 4$	16.6 ± 0.05	107.3 ± 2.0	0.989 ± 0.001
$\mathcal{FV}$	$0 \leq z < 0.5$	18.6 ± 0.03	108.0 ± 3.0	0.989 ± 0.001
	$0.5 \leq z < 1$	18.3 ± 0.05	107.1 ± 1.4	0.988 ± 0.001
	$1 \leq z < 2$	18.2 ± 0.05	107.5 ± 0.9	0.988 ± 0.001
	$2 \leq z < 3$	18.1 ± 0.03	106.9 ± 1.5	0.988 ± 0.001
	$3 \leq z < 4$	18.0 ± 0.04	106.8 ± 0.9	0.988 ± 0.001

$2.3R_G$ ($\approx 14\,h^{-1}$ Mpc) and $r \simeq 2.2R_G$, respectively, which shows that the Gaussian predictions for the maximum position remain relevant down to the mildly non-linear regime.

At large separation, a clearer signature of BAO is seen in the $\mathcal{WW}$ correlation compared to the $\mathcal{PF}$ case. The $\mathcal{WW}$ correlation function shows negligible redshift evolution compared to the peak–filament case. Given the smearing of the BAO feature, the identification of the acoustic scale at late time for $\mathcal{PF}$ is relatively less straightforward, compared to the $\mathcal{WW}$ correlation.

3.4.3 *Angle dependence of cross-correlations: Figs 8–10*

To identify the origin of the characteristic features at $r < 30\,h^{-1}$ Mpc in the peak–filament and wall–void cross-correlation functions, we investigate how the contribution to the correlation depends on the relative orientation of the pair in the eigenframe of the saddle defined by the principal axes of the local Hessian of the density field $H_{ij} = \partial_{ij}\delta$. Indeed, we expect a preferential alignment of the separation vector of the saddle–extrema pair in that frame, given that saddles bridge extrema points together along preferred directions (Bond & Myers 1996; Codis et al. 2017, 2018). In particular, we expect peak–filament pairs to cluster along the direction of positive curvature of the filament saddle and the void–wall pairs along the direction of negative curvature of the wall saddle. In what follows, we will denote $\lambda_1 < \lambda_2 < \lambda_3$ the three ordered eigenvalues of the Hessian matrix and $\boldsymbol{e}_i$ their corresponding eigenvector. We will use the terminology minor axis for $\boldsymbol{e}_3$, intermediate axis for $\boldsymbol{e}_2$, and major axis for $\boldsymbol{e}_1$ such that a filament joining a filament-type saddle and a peak is typically along the minor axis, $\boldsymbol{e}_3$, corresponding to the eigendirection of positive curvature of the saddle. In other words, the minor axis of the density Hessian at filament saddle is, in general, the direction of large-scale filamentary bridges, which drive matter into clusters located at the maxima (peak points) of the density field. On the other hand, it is along the direction of the major axis of the wall's Hessian frame that the inner mass is outflowing from the centre of cosmic voids located at the minima (void points) of the density field.

To first get a global view, Fig. 8 plots the conditional peak (respectively void) overdensity in the 3D frame set by filaments (respectively walls):

$$\frac{\langle n_{\rm ext}|{\rm sad}\rangle}{\overline{n}_{\rm ext}}(\boldsymbol{r}) \equiv \frac{\langle n_{\rm sad}(\boldsymbol{r}_{\rm sad}) n_{\rm ext}(\boldsymbol{r}_{\rm sad} + \mathcal{R}\cdot\boldsymbol{r}))\rangle_{\boldsymbol{r}_{\rm sad}}}{\overline{n}_{\rm ext}\overline{n}_{\rm sad}}, \tag{9}$$

where $\boldsymbol{r}$ is the separation vector in the eigenframe of the saddle, $\boldsymbol{r}_{\rm sad}$ is the position of a saddle point in the simulation frame on which we perform the average, and $\overline{n}$ refers to the mean number density of points (extrema or saddles above threshold). The multiplication by the 3×3 rotation matrix $\mathcal{R} = (\boldsymbol{e}_1, \boldsymbol{e}_2, \boldsymbol{e}_3)$ rotates the position from saddle eigenframe to the Euclidean frame of the simulation. For clarity, we also plot projections of this 3D function on the 2D planes perpendicular to each principal axis of a saddle.

In the left-hand panel, as expected, we find a larger overdensity of peaks along the minor axis, parallel to the eigenvector corresponding to the positive eigenvalue of the Hessian of the density field, λ_3, evaluated at the filament-type saddle point. In particular, when peak overdensities are integrated along the minor axis, we clearly detect a high concentration of peaks along the axis of the filament, and a decreasing number density of peaks in the direction perpendicular to the filament. This is in qualitative agreement with e.g. Codis, Pichon & Pogosyan (2015), Kraljic et al. (2018), Musso et al. (2018), and Bond et al. (1996) that took a peak-centred view arguing for enhanced conditional probability of the filaments in the direction along the peak minor axis, especially between two aligned peaks.

The integration along the major axis confirms the existence of an exclusion zone with a dumbbell shape, showing a clear deficit in the projected peak number density on both sides of the filament and corresponding to two void regions, while this particular signature is less significant when projected along the intermediate axis. This is because peaks are more likely to be found along the intermediate axis corresponding to a wall rather than along the major axis direction. Conversely, we find an excess of voids along the major axis of the Hessian frame of wall-type critical points in the right-hand panel. Similarly, the projected void number density on the plane spanned by the minor and intermediate axes of the wall frame shows a monotonic decrease in the void number density as a function of distance from walls. On other planes, we observe clear exclusion zones, with dumbbell shapes centred on walls. Given that physical structures can be associated with critical points, we can extend this result to the interpretation that large-scale filaments are elongated toward clusters and that walls are facing and surrounding cosmic voids.

More quantitatively, Fig. 9 (respectively Fig. 10) shows the anisotropic contribution to the cross-correlation from different directions identified with respect to each of the principal axis of the filament (respectively wall) Hessian's frame. We calculate the relative counts of critical point pairs with a particular orientation as

$$(1 + \xi_{ij}(\mu, r))\Delta\mu = \frac{\langle C_i C_j(\mu, \mu + \Delta\mu)\rangle}{\sqrt{\langle C_i R_j\rangle\langle C_j R_i\rangle}} \sqrt{\frac{N_{R_j} N_{R_i}}{N_{C_j} N_{C_i}}}, \tag{10}$$

where $\mu \in [0, 1]$ is the cosine of the angle between the principal axis of the saddle frame and the separation vector of that pair, and $\langle C_i C_j(\mu, \mu + \Delta\mu)\rangle$ represents the number of saddle–extremum pairs whose directional cosine is in the range $[\mu, \mu + \Delta\mu]$. The sum of the contributions in equation (10) for all angular bins is exactly the isotropic 2pCF of extrema and saddles. The panels from top to bottom show binned number counts with angles starting from, respectively, the minor, intermediate, and major axis of the saddle. The sum of all bins, identical for each panel, is also shown. Let us remind that for filament saddles, the minor axis points in the most probable direction to the nearest peak, while for wall saddles, the major axis points in the most probable direction of the nearest void (as represented in the schematic guides).

Let us first discuss the near behaviour of the anisotropic contributions to the cross-correlation[7] for peaks and filaments, $ij = \mathcal{FP}$, presented in the left-hand column of Fig. 9. Choosing the directional bin with the highest cosine values ($0.75 \leq \mu \leq 1$) focuses on the close vicinity of a given saddle eigendirection. The bin with the lowest values ($0 \leq \mu < 0.25$) represents a disc, orthogonal to this eigendirection.

The structure of peak number distribution at distances $r \lesssim 30\,h^{-1}$ Mpc is seen to be strikingly different around different axes. The small separation divergence and local maximum feature occur specifically close to the minor axis direction. In the directions misaligned with the minor axis, peak–filament pairs contribute significantly less than the aligned case, and even display some exclusion. This exclusion zone becomes most pronounced when one looks in the plane perpendicular to the minor axis, either in the disc

[7]We should stress that what is plotted are fractional contributions to the total correlation function from the pairs within a given angular separation. As such individual curves should not be interpreted as correlations themselves, in particular the values below unity should not be automatically interpreted as anticorrelation.

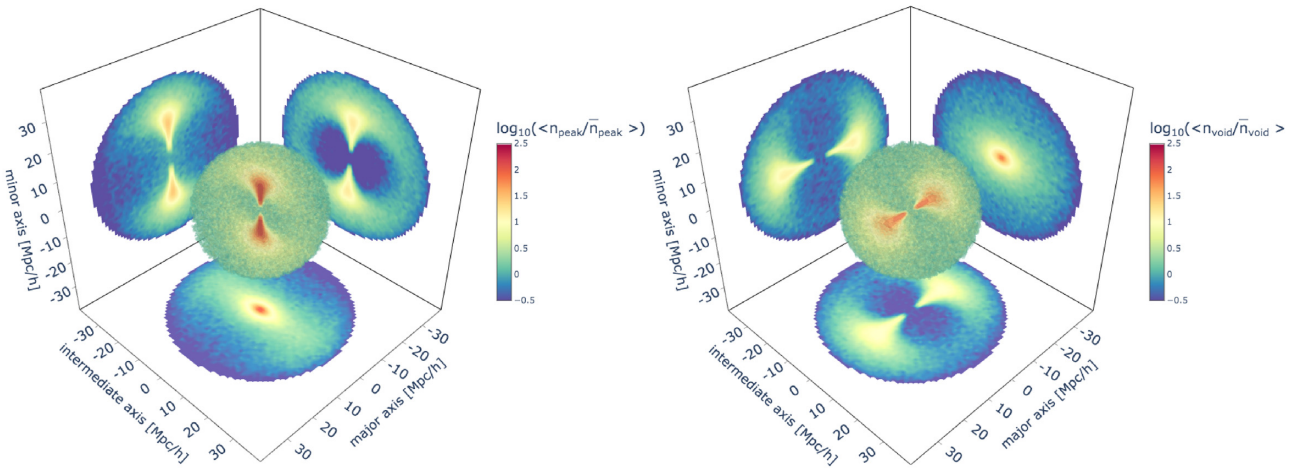

Figure 8. Overdensities of the rarest 20 per cent extrema in the eigenframe of their (20 per cent rarest) saddle points, together with their projection on planes perpendicular to the principal axes of the Hessian, within 30 h^{-1} Mpc of the saddle, as given by equation (9). Peaks around filaments (left) and voids around walls (right) are shown. Excess number densities of peak and void points are found along the minor and major axis of the frame of saddles. Note that the peak (respectively void) number density along this preferential direction (in red) abruptly stops in the vicinity of the saddle point, because it is close to the smoothing scale (6 h^{-1} Mpc) and resolution (2 h^{-1} Mpc) limit. See Fig. A4 for its Gaussian random field theoretical counterpart (which does not suffer from this limitation).

$0 \leq \mu < 0.25$ in the top panel, or in the narrow cones $0.75 \leq \mu \leq 1$ around intermediate and major axes in the middle and bottom panel. This clear anisotropy suggests that peak critical points are distributed primarily along the minor axis of the filament frame, as expected. Along this direction, we expect to find peaks that can be arbitrary close to the filamentary saddle, resulting in a divergence towards zero separation. Fig. 9 shows that this enhancement of peaks around filament comes from a narrow angle range, $0.75 \leq \mu_{\rm min} < 1$, around the minor axis. All other directions display some exclusion zone, more pronounced as μ increases. A more careful analysis, performed on the Gaussian case, shows that the divergence as $r \to 0$ of the $\mathcal{PF}$ cross-correlations exists only for a strictly tangential to minor axis approach to the saddle point $\mu = 0$, all other directions displaying an anticlustering region at small separation. When approaching the saddle point along a ray at a finite non-zero, but sufficiently small angle μ, the $\mathcal{PF}$ correlation exhibits a local maximum at $r \approx 20\,h^{-1}$ Mpc (corresponding to the crossing of the dumbbell contours described previously in the 3D case). When integrated over angles, both features persist, leading to the characteristics shape for the full angle-integrated $\mathcal{PF}$ cross-correlation function discussed earlier that displays both a divergence at small separation and a local maximum.

The dependence of the peak–filament correlation on the orientation is in fact already fully captured in the initial Gaussian random field. Figs A4 and A5 show the Gaussian versions of Fig. 9, together with the projection along the intermediate axis of the filament's frame as in Fig. 8. We show the values of the Gaussian peak–filament correlations in a 2D plane perpendicular to the intermediate axis of the filament frame. There is a good qualitative agreement between the measurement and the Gaussian prediction: stronger clustering along the minor axis, and an axisymmetric exclusion zone near the minor axis. The angular contribution in the right-hand panel of Fig. A4 also matches well the behaviour found in the measurement. The correlation decreases with increasing directional cosine defined with respect to the major axis of filament frame. In particular, the right-hand panel further suggests that the divergence originates predominantly along the direction perpendicular to the major axis (presumably, along the minor axis) and the local maximum in the correlation results from the direction slightly less perpendicular to the major axis (presumably, slightly misaligned with the minor axis).

Note that the features on scales below $r \sim 30\ h^{-1}$ Mpc also change significantly depending on the rarity constraints imposed on critical points. As shown in the left-hand panel of Fig. A5, for cross-correlations of peaks and filaments with different specific rarities, the exclusion zone becomes horizontally elongated, and disconnects high-correlation region since the condition for the critical points to have different rarities makes it unlikely for them to be close to each other. In the right-hand panel, the angular analysis again demonstrates the existence of an exclusion zone in all directions. The extent of the exclusion zone decreases with decreasing alignment to the major axis. On the other hand, the maximum amplitude increases with increased misalignment to the major axis, evidently showing an anisotropic distribution of peak critical points.

Let us now move to BAO scales. In the right-hand panel of Fig. 9, the largest contribution to the cross-correlation still occurs along the minor axis of the saddle frame but also significantly along the intermediate axis. As the separation vector of a pair tilts away from the minor axis of the filament, the relative pair count decreases and falls below the isotropic linear matter case, implying that peak and filament points are anticlustered in all the directions perpendicular to the minor axis. Interestingly, however, it is the major axis that shows the most noticeable BAO feature, as shown in the bottom right-hand panel, which may support the idea that less dense directions may provide a more suitable environment for cosmological analysis. We also note an inversion of the profiles along the intermediate axis (middle row): the highest relative counts at small separation become the lowest on BAO scales.

For the wall–void counts presented in Fig. 10, $ij = \mathcal{WV}$, we find the opposite trend to the peak–filament counts: the main contribution to the divergence and the maximum is produced along the major axis of the wall frame, as can be seen in the bottom left-hand panel. We also detect an exclusion region in the relative counts, when the wall–void separation vector is misaligned ($0 \leq \mu_{\rm maj} < 0.75$) with the major axis. Along the minor and intermediate axes, the pairs with the largest misalignment ($0 \leq \mu < 0.25$) contribute the most. Void critical points are therefore typically located along the direction of

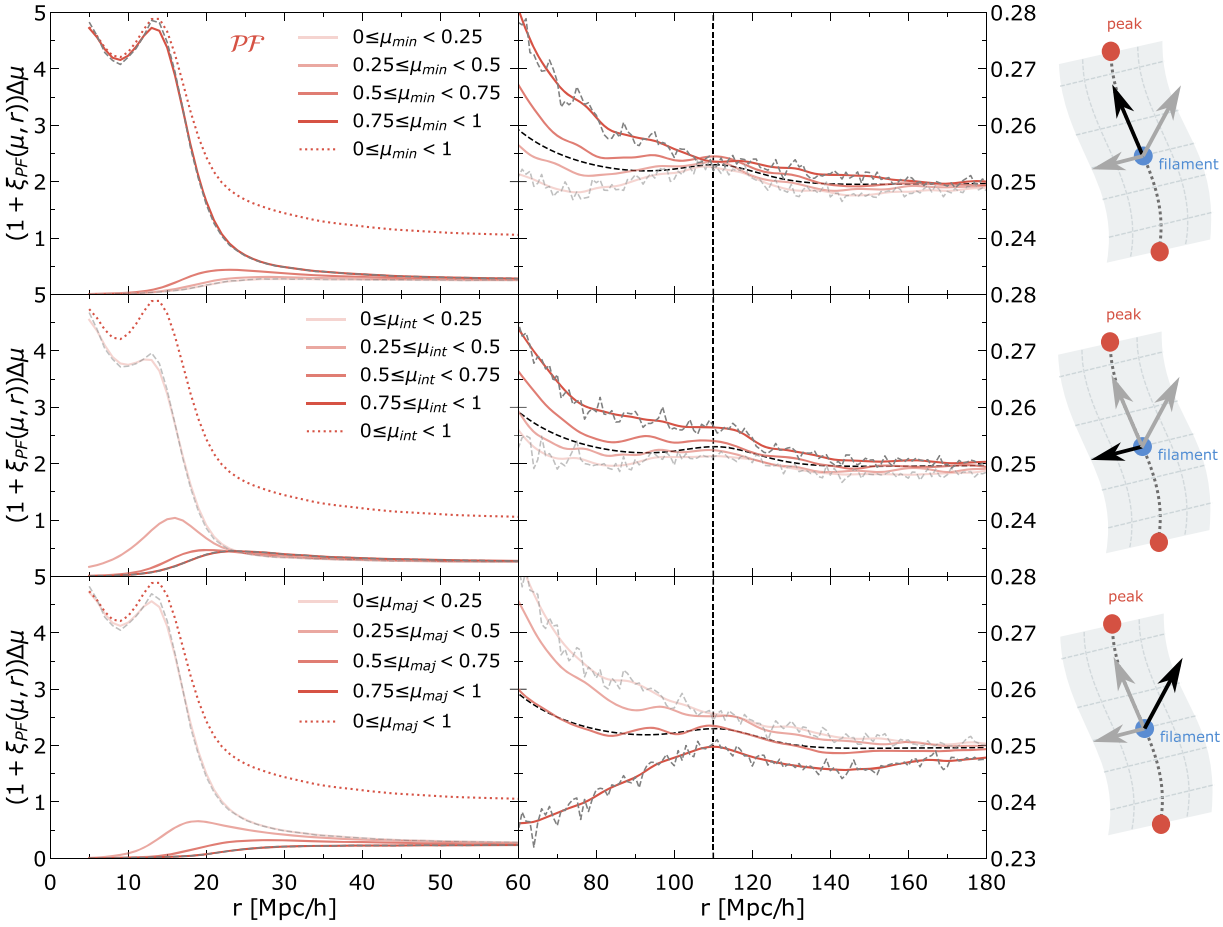

Figure 9. Directional impact on the $\mathcal{PF}$ cross-correlation function for the 20 per cent highest critical points at redshift $0 \le z < 0.5$ for separations between 0 and 60 Mpc h^{-1} (left) and BAO scales (right), as given by equation (10). The impact of the orientation of the separation vector with respect to, respectively, the minor, intermediate, and major axis of the filament's Hessian is presented in, respectively, the top, middle, and bottom panels. A schematic guides showing the reference's direction (black arrow) and the other principal axes (grey arrows) at the saddle point (blue) defining the filament (dashed line connecting two peaks) are also depicted. We also display with a dashed solid line the linear matter correlation multiplied by the same factor of 8 as before and divided by 4 (which is the number of bins of angles). The vertical line marks the position of the BAO in the linear matter correlation. In the top panel, the small-scale contribution to the $\mathcal{PF}$ correlation comes mostly from the direction along the minor axis ($0.75 \le \mu_{\rm min} < 1$) of the eigenframe, which implies that peaks are preferentially located along the filament's principal axis, as expected (Codis et al. 2018). The rest of the orientations shows an exclusion zone. For the middle (respectively bottom) panel, a major contribution at small separation originates from the direction perpendicular to the intermediate (respectively major) axis of the filament frame. This is qualitatively consistent with the 3D counts shown in Fig. 8, left-hand panel. At large separation, it is still the direction along the minor axis of the filament that contributes most to the correlation in the top right-hand panel. Although the correlation along the major axis is the minimum, it displays the most noticeable BAO feature at large separation.

the major axis of the wall frame, as expected, and create a divergence at zero separation. The sum of this behaviour with exclusions along all the other directions creates the typical local maximum observed for the isotropic case. We once again note an inversion of the profiles, this time along the minor axis (top row): the highest relative counts at small separation become the lowest on BAO scales. We also note that for Gaussian random fields, this case is symmetric to the peak–filament correlation and therefore can be explained in a dual fashion.

In the right-hand panels of Fig. 10, the behaviour at large separation is different from the peak–filament case. Previously, the most significant BAO feature appeared along the major axis, although the dominant amplitude contribution to the isotropic correlation function came from the minor axis. In the present case, the BAO signature is more clearly detected along the intermediate axis, as can be seen in the middle right-hand panel. Note that the largest contribution at small separation occurs along the major axis.

4 THE AVERAGE COSMIC CRYSTAL

The features in the measured and predicted cross-correlation functions, and first of all the existence of the clear local maximum of the cross-correlations at $r \approx 13$–$15\ h^{-1}$ Mpc, indicate that critical points are not uniformly located but exhibit on average a regular pattern in their spatial distribution (Pichon et al. 2010; Codis et al. 2018; Cadiou et al. 2020).

Thus, we examine the relative position of critical points traced by the maxima of their cross-correlations to investigate how the critical points are spatially distributed by finding their characteristic clustering scale. Here we are interested in the most prominent features of the cosmic web – densest peaks, filaments, and walls. We also select the densest voids as they may correspond to the interior of the densest walls and voids are often defined by their boundary. Here, in practice, we restrict the sample of critical points to their respective highest 20 per cent range.

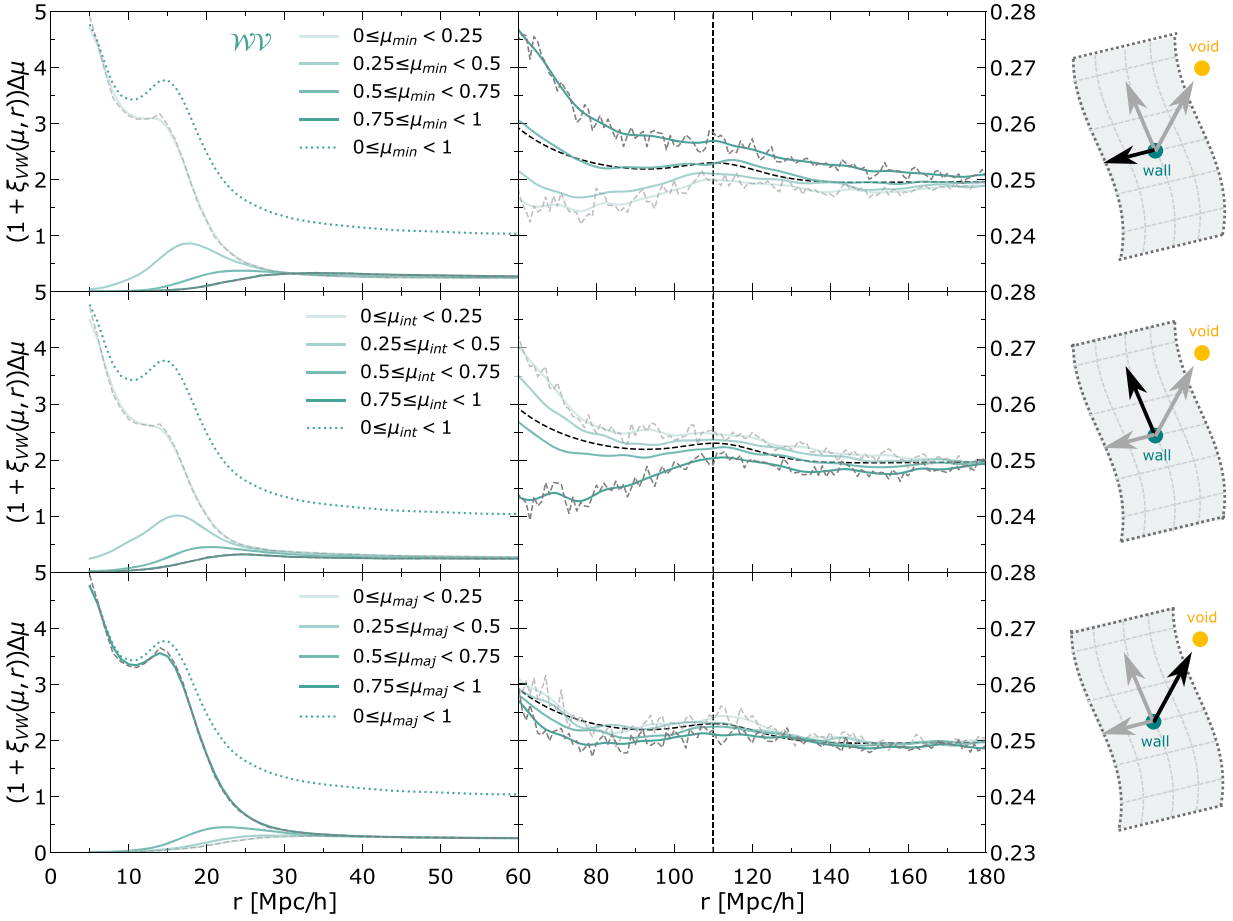

Figure 10. Directional contribution to the $\mathcal{WW}$ cross-correlation function of the 20 per cent lowest critical points for $0 \le z < 0.5$ for separations between 0 and 60 Mpc h^{-1} (left) and BAO scales (right), as given by equation (10). Different orientation with respect to the minor, intermediate, and major axis of the wall Hessian are presented from the top to the bottom panel. A schematic guides showing the reference direction (black arrow) defining the frame (grey arrows) are also depicted. We also display with a dashed solid line the linear matter correlation multiplied by the same 'bias' factor of 8 as before and divided by 4 (which is the number of bins of cosines). The vertical line marks the position of the BAO in the linear matter correlation. In the bottom panel, the small-scale contribution to the $\mathcal{WW}$ correlation mostly comes from the direction along the major axis ($0.75 \le \mu_{\rm max} < 1$) of the wall eigenframe, which implies that voids are preferentially located around the wall saddle point, in analogy to the $\mathcal{PF}$ case (Fig. 9). See also the 3D counts in Fig. 8, right-hand panel. At large separation, the BAO signature is more pronounced along the wall's intermediate axis.

The top panel of Fig. 11 shows the redshift evolution of the correlations between peaks and the other critical points. We find that the typical peak-to-filament distance (as given by the position of the local maximum) is ∼0.7 times the peak-to-wall most likely distance and ∼0.6 times the peak-to-void separation. Remarkably, this is very close to the factors $1/\sqrt{2}$ and $1/\sqrt{3}$ expected in a cubic-centred lattice. These ratios remain nearly constant during the evolution. For the 5 per cent highest critical points, the ratios slightly increase to $r_{\mathcal{PF}}/r_{\mathcal{PW}} \approx 0.73$ and $r_{\mathcal{PF}}/r_{\mathcal{PV}} \approx 0.63$, but also in this case there is little redshift variation. So it appears that the cosmic web through its evolution *on average* bears similarities with a cubic lattice with the peak at the centre of the cube, filament-type saddles at the centre of the faces, wall-type saddles at the centre of the ridges, and voids at the corners as in the bottom panel of Fig. 11, which shows a qualitative rendering of the corresponding crystal, consistent with these ratios. This is consistent with the connectivity of the cosmic web in the initial conditions presented in Appendix A5 and investigated by Codis et al. (2018) (see also Darragh Ford et al. 2019; Kraljic et al. 2020, for observational evidence). Note importantly that in practice the vicinity of each peak does not typically have this geometry: the regularity only arises because we investigate the mean field around them and therefore average out all fluctuations around it. Most peaks are in fact dominated by one massive wall and two or three massive embedded filaments (Pichon et al. 2011; Codis et al. 2018).

From a cosmological perspective, the relative insensitivity to redshift evolution of the 'cosmic crystal' suggests it could possibly be used as a standard ruler, e.g. to constrain the equation of state of dark energy, or to carry out an Alcock–Paczynski test (Nusser 2005; Blake et al. 2011b; Park et al. 2019). Note that the crystal centred on the voids is dual to that centred on the peaks (see Fig. A6, bottom panel). Note finally that given the relative insensitivity to non-linearities of saddle points specifically, it might be worth considering the clustering of saddles (Figs 6 and B1) as a more robust quantity to model. However, let us emphasize that the choice of considering the densest critical points (especially for voids) may not be the most realistic ones. We defer a thorough analysis of the cosmic crystal in realistic set-ups to future investigations.[8]

[8]In particular, an analysis of the crystal as a function of the persistence of the cosmic web (Sousbie 2011) would be an interesting avenue of research.

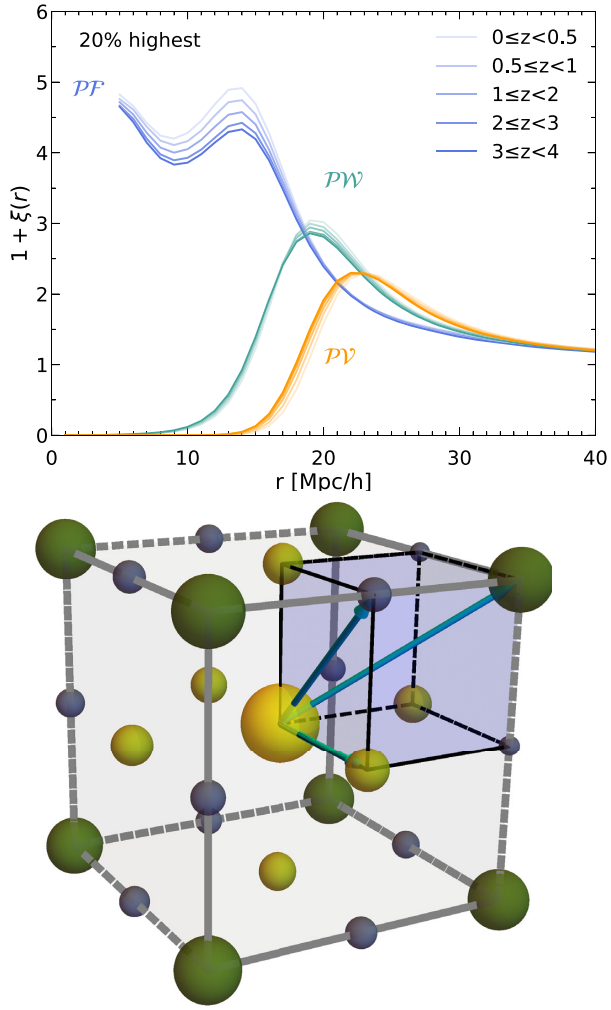

Figure 11. Redshift evolution of the correlations between peaks and different critical points as labelled, all in their 20 per cent highest rarity bin (top). Measured radii ratios are consistent with the Gaussian case shown in Fig. A6 as $r_{\mathcal{PF}}/r_{\mathcal{PW}} = 0.7$ and $r_{\mathcal{PF}}/r_{\mathcal{PV}} = 0.6$. These radii ratios in turn suggest that the cosmic web has (on average) a cosmic cubic-centred crystal structure as shown (bottom). Here, the peak is represented as a big yellow sphere, the filament saddle as green spheres, the wall saddles as small blue spheres, and the voids as big light green spheres. The blue arrows lengths are respectively $r_{\mathcal{PF}}$, $r_{\mathcal{PW}}$, and $r_{\mathcal{PV}}$.

5 CONCLUSIONS AND PERSPECTIVES

5.1 Conclusions

Focusing on both small-to-intermediate separations and BAO scales, the cosmic evolution of the clustering properties of peak, void, wall, and filament critical points of fixed abundance was measured using 2pCFs in ΛCDM dark matter simulations as a function of redshift. The two-point functions involving less non-linear critical points – wall and filament saddle points – proved more insensitive to redshift evolution, which may prove advantageous from a modelling perspective in the context of dark energy experiments. This conclusion is perfectly in line with the findings of Gay et al. (2012) for one-point statistics.

A qualitative comparison to the corresponding theory for Gaussian random fields (see Appendix A) allowed us to understand the following features.

(i) The appearance of an exclusion zone at small separation whose size increases with rarity and which depends on the signature difference between the critical points.

(ii) The divergence-and-maximum of cross-correlations of peaks and filament-type saddles (respectively voids and wall-type saddles), reflecting the relative loci of such points along filaments (respectively walls), as expected from critical event theory (Cadiou et al. 2020).

(iii) The amplification of the BAO bump with the rarity of the critical points for autocorrelations, which corresponds to a dip for cross-correlations involving one negative bias factor.

(iv) The robustness of the observed location of the inflection point at $r \simeq 134 \pm 3\,h^{-1}$ Mpc corresponding to zero correlation in all pairs of critical points, which interestingly does not seem to depend on bias or redshift.

(v) The relative insensitivity to redshift evolution of the 'cosmic crystal', which suggests it could possibly be used as a standard ruler.

The qualitative agreement between the simulations on the one hand and the predictions for Gaussian random fields on the other hand is striking given the level of non-linearity probed ($\sigma \sim 0.6$). This suggests that on the scales probed in this paper, the relative clustering of critical points was already encoded in the initial conditions (Pogosyan et al. 1998) and is conserved throughout the cosmic evolution.

Note that Tables 3 and 5 quantified the characteristic scales and amplitude of these correlations as a function of rarity, and their redshift evolutions including BAO are summarized in Tables 4 and 6, when relevant.

5.2 Perspectives

As a first systematic investigation of two-point functions of other critical points (beyond peaks and void), this work is obviously non-exhaustive. In this paper, we only touched upon the properties of the two-point functions in the vicinity of the BAO scale, in contrast to the vast literature available for peaks, and the more limited work on voids (e.g. Kitaura et al. 2016). Extending some of this work to other critical points should be a priority in the future, in particular given their relative insensitivity to cosmic evolution. Beyond the scope of this paper, it would be interesting to also quantify the two-point functions of critical points in 2D intensity maps (Madau, Meiksin & Rees 1997; Bull et al. 2015; Smoot & Debono 2017) or weak lensing maps (Abbott et al. 2018). It would also be of interest to extend the Gaussian random field predictions of Appendix A taking into account the Zeldovich displacements of critical points (Regos & Szalay 1995) and/or introduce non-Gaussian corrections via a Gram–Charlier expansion of the joint PDFs, extending to two-point functions the results of Gay et al. (2012) and equation (8). This would allow us to model the redshift evolution (Sections 3.3.2 and 3.4.2) and construct the corresponding estimators for dark energy experiments. The density fields could then for instance be extracted from upcoming Lyα tomographic reconstructions (Pichon et al. 2001; Lee et al. 2014) applied to wide field surveys like PFS or WEAVE. It would eventually be worthwhile to also quantify the three-point functions of critical points. One could also investigate how modified gravity or primordial non-Gaussianities impact the clustering of these critical points (Falck et al. 2018; Dvorkin et al. 2019).

ACKNOWLEDGEMENTS

We thank an anonymous referee for helpful comments that helped improve the original manuscript. JS is supported by a KIAS In-

dividual Grant (PG071202) at the Korea Institute for Advanced Study. DP acknowledges a visiting fellowship from KIAS during his visit in Seoul when this project was initiated. SC acknowledges support from the SPHERES grant ANR-18-CE31-0009 of the French Agence Nationale de la Recherche and from Fondation Merac. CC is sponsored by the European Union Horizon 2020 Framework Programme, under grant agreement no. 818085 GMGalaxies. This work has made use of the Horizon Cluster hosted by Institut d'Astrophysique de Paris. We thank Stéphane Rouberol for running smoothly this cluster for us. This work was partially supported by the Segal grant ANR-19-CE31-0017 (secular-evolution.org) of the French Agence Nationale de la Recherche.

DATA AVAILABILITY

The data underlying this paper are available in the paper and in its online supplementary material.

REFERENCES

Abbott T. M. C. et al., 2018, Phys. Rev. D, 98, 043526
Anselmi S., Starkman G. D., Sheth R. K., 2015, MNRAS, 455, 2474
Arnold V. I., 2006, Ordinary Differential Equations. Springer-Verlag, Berlin
Bahcall N. A., Soneira R. M., 1983, ApJ, 270, 20
Baker T., Clampitt J., Jain B., Trodden M., 2018, Phys. Rev. D, 98, 023511
Baldauf T., Desjacques V., 2017, Phys. Rev. D, 95, 043535
Baldauf T., Codis S., Desjacques V., Pichon C., 2016, MNRAS, 456, 3985
Baldauf T., Codis S., Desjacques V., Pichon C., 2020, preprint (arXiv:2012.14404)
Banerjee A., Dalal N., 2016, J. Cosmol. Astropart. Phys., 11, 015
Bardeen J. M., Bond J. R., Kaiser N., Szalay A. S., 1986, ApJ, 304, 15
Barreira A., Cautun M., Li B., Baugh C. M., Pascoli S., 2015, J. Cosmol. Astropart. Phys., 08, 028
Bernardeau F., Kofman L., 1995, ApJ, 443, 479
Bernardeau F., Pichon C., Codis S., 2014, Phys. Rev. D, 90, 103519
Beutler F. et al., 2011, MNRAS, 416, 3017
Blake C. et al., 2011a, MNRAS, 418, 1707
Blake C. et al., 2011b, MNRAS, 418, 1725
Bond J. R., Myers S. T., 1996, ApJS, 103, 1
Bond J. R., Cole S., Efstathiou G., Kaiser N., 1991, ApJ, 379, 440
Bond J. R., Kofman L., Pogosyan D., 1996, Nature, 380, 603
Bull P., Ferreira P. G., Patel P., Santos M. G., 2015, ApJ, 803, 21
Cadiou C., Pichon C., Codis S., Musso M., Pogosyan D., Dubois Y., Cardoso J. F., Prunet S., 2020, MNRAS, 496, 4787
Cai Y.-C., Padilla N., Li B., 2015, MNRAS, 451, 1036
Chan K. C., Hamaus N., Desjacques V., 2014, Phys. Rev. D, 90, 103521
Clampitt J., Cai Y.-C., Li B., 2013, MNRAS, 431, 749
Clampitt J., Jain B., Sánchez C., 2016, MNRAS, 456, 4425
Codis S., Pichon C., Pogosyan D., 2015, MNRAS, 452, 3369
Codis S., Gavazzi R., Pichon C., Gouin C., 2017, A&A, 605, A80
Codis S., Pogosyan D., Pichon C., 2018, MNRAS, 479, 973
Crocce M., Scoccimarro R., 2008, Phys. Rev. D, 77, 023533
Darragh Ford E. et al., 2019, MNRAS, 489, 5695
Davis M., Peebles P. J. E., 1983, ApJ, 267, 465
Desjacques V., 2008, Phys. Rev. D, 78, 103503
Desjacques V., 2013, Phys. Rev. D, 87, 043505
Desjacques V., Crocce M., Scoccimarro R., Sheth R. K., 2010, Phys. Rev. D, 82, 103529
Desjacques V., Jeong D., Schmidt F., 2018, Phys. Rep., 733, 1
Dvorkin C. et al., 2019, BAAS, 51, 64
Eisenstein D. J., Hu W., 1998, ApJ, 496, 605
Estrada J., Sefusatti E., Frieman J. A., 2009, ApJ, 692, 265
Falck B., Koyama K., Zhao G.-B., Cautun M., 2018, MNRAS, 475, 3262
Fard M. A., Taamoli S., Baghram S., 2019, MNRAS, 489, 900
Font-Ribera A. et al., 2014, J. Cosmol. Astropart. Phys., 05, 027
Gay C., Pichon C., Pogosyan D., 2012, Phys. Rev. D, 85, 023011
Gaztañaga E., Norberg P., Baugh C. M., Croton D. J., 2005, MNRAS, 364, 620
Gil-Marín H. et al., 2015, MNRAS, 452, 1914
Hamaus N., Wandelt B. D., Sutter P. M., Lavaux G., Warren M. S., 2014, Phys. Rev. Lett., 112, 041304
Hamaus N., Sutter P. M., Lavaux G., Wandelt B. D., 2015, J. Cosmol. Astropart. Phys., 11, 036
Hamaus N., Pisani A., Sutter P. M., Lavaux G., Escoffier S., Wandelt B. D., Weller J., 2016, Phys. Rev. Lett., 117, 091302
Hamaus N., Cousinou M.-C., Pisani A., Aubert M., Escoffier S., Weller J., 2017, J. Cosmol. Astropart. Phys., 07, 014
Hawkins E. et al., 2003, MNRAS, 346, 78
Kaiser N., 1984, ApJ, 284, L9
Kaiser N., 1986, MNRAS, 222, 323
Kaiser N., 1991, ApJ, 383, 104
Kitaura F.-S. et al., 2016, Phys. Rev. Lett., 116, 171301
Kraljic K. et al., 2018, MNRAS, 474, 547
Kraljic K. et al., 2020, MNRAS, 491, 4294
Kreisch C. D., Pisani A., Carbone C., Liu J., Hawken A. J., Massara E., Spergel D. N., Wandelt B. D., 2019, MNRAS, 488, 4413
Kulkarni G. V., Nichol R. C., Sheth R. K., Seo H.-J., Eisenstein D. J., Gray A., 2007, MNRAS, 378, 1196
Lares M., Ruiz A. N., Luparello H. E., Ceccarelli L., Garcia Lambas D., Paz D. J., 2017, MNRAS, 468, 4822
Lee K.-G. et al., 2014, ApJ, 795, L12
Li B., Zhao G.-B., Koyama K., 2012, MNRAS, 421, 3481
Liang Y., Zhao C., Chuang C.-H., Kitaura F.-S., Tao C., 2016, MNRAS, 459, 4020
Liu Y., Liang Y., Yu H.-R., Zhao C., Qin J., Zhang T.-J., 2017, preprint (arXiv:1712.01002)
Ludlow A. D., Porciani C., 2011, MNRAS, 413, 1961
McDonald P., Eisenstein D. J., 2007, Phys. Rev. D, 76, 063009
Madau P., Meiksin A., Rees M. J., 1997, ApJ, 475, 429
Marulli F. et al., 2018, A&A, 620, A1
Massara E., Villaescusa-Navarro F., Viel M., Sutter P. M., 2015, J. Cosmol. Astropart. Phys., 11, 018
Matsubara T., Codis S., 2020, Phys. Rev. D, 101, 063504
Milnor J., 1963, Morse Theory. Princeton Univ. Press, Princeton, NJ
Musso M., Cadiou C., Pichon C., Codis S., Kraljic K., Dubois Y., 2018, MNRAS, 476, 4877
Nusser A., 2005, MNRAS, 364, 743
O'Dwyer M., Anselmi S., Starkman G. D., Corasaniti P.-S., Sheth R. K., Zehavi I., 2020, Phys. Rev. D, 101, 083517
Padilla N. D., Ceccarelli L., Lambas D. G., 2005, MNRAS, 363, 977
Park H., Park C., Sabiu C. G., Li X.-d., Hong S. E., Kim J., Tonegawa M., Zheng Y., 2019, ApJ, 881, 146
Paz D., Lares M., Ceccarelli L., Padilla N., Lambas D. G., 2013, MNRAS, 436, 3480
Peacock J. A., Heavens A. F., 1985, MNRAS, 217, 805
Peebles P. J. E., 1970, AJ, 75, 13
Peebles P. J. E., 1981, ApJ, 243, L119
Percival W. J. et al., 2010, MNRAS, 401, 2148
Pichon C., Vergely J. L., Rollinde E., Colombi S., Petitjean P., 2001, MNRAS, 326, 597
Pichon C., Gay C., Pogosyan D., Prunet S., Sousbie T., Colombi S., Slyz A., Devriendt J., 2010, in Alimi J.-M., Fuözfa A., eds, AIP Conf. Proc. Vol. 1241, Invisible Universe: Proceedings of the Conference. Am. Inst. Phys., New York, p. 1108
Pichon C., Pogosyan D., Kimm T., Slyz A., Devriendt J., Dubois Y., 2011, MNRAS, 418, 2493
Pisani A., Sutter P. M., Hamaus N., Alizadeh E., Biswas R., Wandelt B. D., Hirata C. M., 2015, Phys. Rev. D, 92, 083531
Pogosyan D., Bond J. R., Kofman L., Wadsley J., 1998, in Colombi S., Mellier Y., Raban B., eds, Wide Field Surveys in Cosmology. Editions Frontieres, Groningen, the Netherlands, p. 61
Pogosyan D., Pichon C., Gay C., Prunet S., Cardoso J. F., Sousbie T., Colombi S., 2009, MNRAS, 396, 635
Press W. H., Schechter P., 1974, ApJ, 187, 425

Regaldo-Saint Blancard B., Codis S., Bond J. R., Stein G., 2021, preprint (arXiv:2101.01455)
Regos E., Szalay A. S., 1995, MNRAS, 272, 447
Ruiz A. N., Paz D. J., Lares M., Luparello H. E., Ceccarelli L., Lambas D. G., 2015, MNRAS, 448, 1471
Schuster N., Hamaus N., Pisani A., Carbone C., Kreisch C. D., Pollina G., Weller J., 2019, J. Cosmol. Astropart. Phys., 12, 055
Sheth R. K., van de Weygaert R., 2004, MNRAS, 350, 517
Shim J., Park C., Kim J., Hwang H. S., 2020, ApJ, in press (arXiv:2012.03511)
Smoot G. F., Debono I., 2017, A&A, 597, A136
Sousbie T., 2011, MNRAS, 414, 350
Sousbie T., Pichon C., Colombi S., Novikov D., Pogosyan D., 2008, MNRAS, 383, 1655
Sousbie T., Colombi S., Pichon C., 2009, MNRAS, 393, 457
Spolyar D., Sahlén M., Silk J., 2013, Phys. Rev. Lett., 111, 241103
Springel V., Yoshida N., White S. D. M., 2001, New Astron., 6, 79
Stopyra S., Peiris H. V., Pontzen A., 2021, MNRAS, 500, 417
Uhlemann C., Codis S., Kim J., Pichon C., Bernardeau F., Pogosyan D., Park C., L'Huillier B., 2017, MNRAS, 466, 2067
Veropalumbo A., Marulli F., Moscardini L., Moresco M., Cimatti A., 2016, MNRAS, 458, 1909
Verza G., Pisani A., Carbone C., Hamaus N., Guzzo L., 2019, J. Cosmol. Astropart. Phys., 12, 040
Voit G. M., 2005, Rev. Modern Phys., 77, 207
Voivodic R., Lima M., Llinares C., Mota D. F., 2017, Phys. Rev. D, 95, 024018

APPENDIX A: THEORY FOR GAUSSIAN RANDOM FIELDS

In order to enlighten the measurements presented in the main text, let us make Lagrangian predictions for the correlation of critical points in Gaussian random fields. We will first predict the auto- and cross-correlations for Gaussian random fields, and investigate the variation of the cross-correlation between peaks and filament saddle points in the frame of the Hessian of the saddle as a function of orientation. Finally, we will highlight the geometry of the so-called cosmic crystal that we can infer from these correlations.

A1 Gaussian peak statistics

Let us define the two-point correlation of all critical points based on the joint statistics of the field and its successive derivatives. From the joint two-point statistics, we can define the excess probability $\xi_{pq}(r, \nu_1, \nu_2)$ of having critical points of kind $p, q \in (\mathcal{P}, \mathcal{F}, \mathcal{W}, \mathcal{V})$ of the field at height higher (for critical points with negative signature – peaks and filament – lower for the ones with positive signatures – walls and voids) than ν_1 and ν_2, smoothed at scales R and located at positions $(\boldsymbol{r}_x, \boldsymbol{r}_y)$, as

$$1 + \xi_{pq}(r|\nu_1, \nu_2) = \frac{\langle \mathrm{cond}_p(\boldsymbol{x}) \times \mathrm{cond}_q(\boldsymbol{y})\rangle}{\langle \mathrm{cond}_p(\boldsymbol{x})\rangle \langle \mathrm{cond}_q(\boldsymbol{x})\rangle}, \tag{A1}$$

where $\boldsymbol{x} = \{x, x_i, x_{ij}\}$ (respectively $\boldsymbol{y}$) is the set of fields at location $\boldsymbol{r}_x$ (respectively $\boldsymbol{r}_y$), and $r = |\boldsymbol{r}_x - \boldsymbol{r}_y|$ the spatial separation between the two points. Here the field and its successive derivatives have been divided by their respective rms: $x = \delta/\sigma_0$, $x_i = \nabla_i\delta/\sigma_1$, and $x_{ij} = \nabla_i\nabla_j\delta/\sigma_2$, where

$$\sigma_i^2(R) \equiv \frac{1}{2\pi^2}\int_0^\infty \mathrm{d}k k^2 P_k(k) k^{2i} W^2(kR) \tag{A2}$$

(with P_k the underlying power spectrum, and W the Gaussian filter), so that we have $\langle x^2\rangle = \sum_k \langle x_k^2\rangle = \langle \left(\sum_k x_{kk}\right)^2\rangle = 1$.

Evaluating the expectation in equation (A1) requires the full knowledge of the joint statistics of the field $P(\boldsymbol{x}, \boldsymbol{y})$ (involving $(1 + 3 + 6) \times 2 = 20$ variables), given by

$$P(\boldsymbol{x}, \boldsymbol{y}) = \frac{\exp\left[-\frac{1}{2}\begin{pmatrix}\boldsymbol{x}\\ \boldsymbol{y}\end{pmatrix}^{\mathrm{T}} \cdot \mathbf{C}^{-1} \cdot \begin{pmatrix}\boldsymbol{x}\\ \boldsymbol{y}\end{pmatrix}\right]}{\det|\,(2\pi)\,\mathbf{C}|^{1/2}}, \tag{A3}$$

where $\mathbf{C}$ is the covariance matrix that depends on the separation vector only because of homogeneity:

$$\mathbf{C} = \begin{pmatrix}\mathbf{C}_{xx} & \mathbf{C}_{xy}\\ \mathbf{C}_{xy}^{\mathrm{T}} & \mathbf{C}_{yy}\end{pmatrix}. \tag{A4}$$

Note that the correlation length of the various components of $\mathbf{C}_{xy}$ differ, as higher derivatives decorrelate faster. Equation (A1) evaluates the function $\mathrm{cond}_i(\boldsymbol{x})$, which for instance, for peaks, $p = P$, obeys (Bardeen et al. 1986)

$$\mathrm{cond}_P(\boldsymbol{x}) = \delta_{\mathrm{D}}^{(3)}(x_i)|\det(x_{ik})|\Theta_{\mathrm{H}}(-\det(x_{ik})) \times \Theta_{\mathrm{H}}(-\mathrm{tr}(x_{ik}))\Theta_{\mathrm{H}}(\mathrm{tr}^2(x_{ik}) - \mathrm{tr}(x_{il}x_{lk})), \tag{A5}$$

where the three Heaviside conditions ensure that the determinant and the trace are negative while the minor is positive so that the three eigenvalues are negative. Similar conditions hold for the other critical points.

In practice we rely on Monte Carlo methods in MATHEMATICA in order to evaluate numerically equation (A1). Namely, we draw random numbers from the conditional probability that $\boldsymbol{x}$ and $\boldsymbol{y}$ satisfy the joint PDF (A3), subject to the condition that $x_j = y_j = 0$, $x > \nu_1$ and $y > \nu_2$ (respectively $<$ for walls and voids). For each draw $(\boldsymbol{x}^{(\alpha)}, \boldsymbol{y}^{(\alpha)})$, $\alpha = 1, \ldots, N$, we drop or keep the sample, depending on the signs of $x^{(\alpha)} - \nu$, $y^{(\alpha)} - \nu$, and the eigenvalues of $(x_{ik}^{(\alpha)})$ and $(y_{ik}^{(\alpha)})$. If it is kept, we evaluate $\det\left(x_{ik}^{(\alpha)}\right)\det\left(y_{ik}^{(\alpha)}\right)$. Then, an estimate for the numerator of equation (A1) reads

$$\langle \mathrm{cond}_p(\boldsymbol{x})\mathrm{cond}_p(\boldsymbol{y})\rangle \approx \frac{P_{\mathrm{m}}(x_i = y_k = 0)}{N}\sum_{\alpha\in\mathcal{S}_{pq}}\left|\det\left(x_{ik}^{(\alpha)}\right)\det\left(y_{ik}^{(\alpha)}\right)\right|,$$

where N is the total number of draws, P_{m} the marginal probability for the field gradients, and $\mathcal{S}_{pq}$ is the subset of the indices of draws satisfying the constraints p, q on the Hessians and the densities at separation $\boldsymbol{r}$. The same procedure can be applied to evaluate expectation entering the denominator of equation (A1),

$$\langle \mathrm{cond}_p(\boldsymbol{x})\rangle \approx \frac{P_{\mathrm{m}}(x_i = 0|r)}{N}\sum_{\alpha\in\mathcal{S}_p}\left|\det\left(x_{ik}^{(\alpha)}\right)\right|,$$

which then yields an estimation of $\xi_{pq}(r, \nu_1, \nu_2)$. This algorithm is embarrassingly parallel.

A2 Isotropic clustering of critical points

Fig. A1 shows predictions for all the cross-correlations and for an abundance of 15 per cent, while Fig. A2 displays the peak and filament autocorrelation and Fig. A3 shows the peak–filament cross-correlation function for various abundances. To get these results, we employed a power-law power spectrum with spectral index $n_{\mathrm{s}} = -1.5$ that is close to a ΛCDM power spectrum at the scales probed in this paper. In principle, similar calculations – although more computing time-consuming – could be performed in this case but would not change significantly the result. The $\mathcal{PF}$, $\mathcal{FF}$, and $\mathcal{PP}$ 2pCFs are found to display a maximum at a few smoothing lengths (with decreasing amplitude in this order) before decreasing asymptotically towards 0 at large separations. The $\mathcal{PF}$ diverges as r

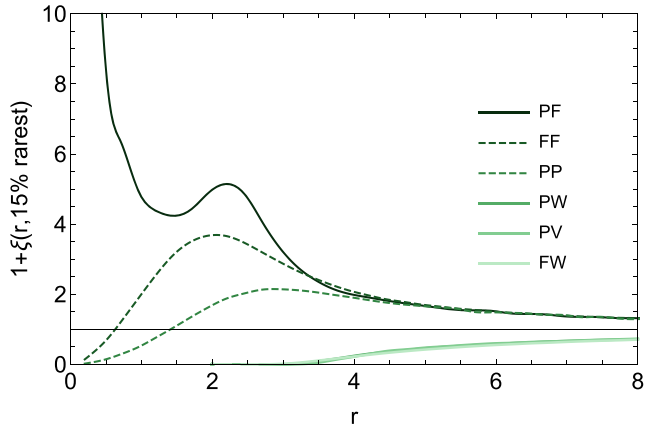

Figure A1. Auto (dashed) and cross (solid) 2pCFs as a function of the separation in units of the (arbitrary) smoothing length, for Gaussian random field with $n_s = -1.5$ and for an abundance of 15 per cent. Note that the curves for $\mathcal{PW}$, $\mathcal{PV}$, and $\mathcal{FW}$ correlations are almost indistinguishable on this plot. The correlations are qualitatively consistent with the measurements in simulations presented in the main text (Figs 2, 4, and 5).

$\to 0$, as expected since one can find infinitely close peak–filament pair without having unlikely constraints to fulfil such as a critical point of another kind in between. This is not the case for $\mathcal{PP}$ (respectively $\mathcal{FF}$) that have to go to -1 at zero separation as one needs to go through a filament saddle (respectively a peak or a wall-type saddle) between the two components of the pair. On the other hand, the $\mathcal{PW}$, $\mathcal{PV}$, and $\mathcal{FW}$ 2pCFs are almost identical: they are always negative, with an extended exclusion zone at small separations followed by a monotonic growth towards $\xi = 0$ at infinity. The respective extent of their exclusion zone is ordered in the same way as in the simulation. All correlations show qualitatively consistent features with the measured 2pCFs at redshift zero (Figs 2, 4, and 5).

For auto 2pCF as a function of the abundance (Fig. A2), the shape and amplitude match qualitatively the non-linearly evolved correlations presented in the main text (Fig. 2, top and middle left-hand panels). As expected, the rarer the critical points, the more biased the tracers and the larger the amplitude of the 2pCF. The same conclusion holds for the $\mathcal{PF}$ 2pCF in Fig. A3, which should be compared to the top left-hand panel of Fig. 5.

In all cases, we note that the predicted correlation function is always larger for rarer critical points, a feature consistent with the findings on evolved simulations reported in the main text, which in itself is remarkable, given the level of non-linearity probed ($\sigma \sim 0.6$). Also note that for Gaussian random fields, rare peaks (above a given threshold) have the exact same behaviour as rare void (below the same threshold with opposite sign) and rare filaments are equivalent to rare walls (due to the field symmetry $\delta \to -\delta$) that is why we only display a subset of all correlation functions, the rest being redundant (for instance $\mathcal{W}$ is identical to $\mathcal{PP}$).

A3 Oriented clustering

Fig. A4 then shows predictions for the $\mathcal{PF}$ cross-correlation in the frame of the saddle using Gaussian random field. For that purpose, we adopt the same algorithmic strategy as described in Regaldo-Saint Blancard et al. (2021), but replacing the orientation of the tidal tensor used there by the orientation of the density Hessian. This is achieved by adding in equation (A5) the constraint

$$\mathcal{B}(\boldsymbol{X}) = 2\pi^2(x_{33}-x_{22})(x_{22}-x_{11})(x_{33}-x_{11})\delta_{\rm D}(x_{12}) \times \delta_{\rm D}(x_{13})\delta_{\rm D}(x_{23})\Theta_{\rm H}(x_{33}-x_{22})\Theta_{\rm H}(x_{22}-x_{11}), \quad \text{(A6)}$$

which allows us to impose the off-diagonal coefficients of the density Hessian to be zero, the curvatures to be ordered and to add the Jacobian of the transformation from arbitrary frame to the frame of the density Hessian by means of the usual Vandermonde determinant $(x_{33}-x_{22})(x_{22}-x_{11})(x_{33}-x_{11})$ with an additional $2\pi^2$ due to the integration over the Euler angles.

The result for the $\mathcal{PF}$ cross-correlation for the 20 per cent highest points in the frame of the saddle is displayed in Fig. A4 for again a spectral index $n_s = -1.5$ and the separation is shown in units of the (arbitrary) smoothing length. The resolution is 10 per cent of the smoothing length, hence the artefact close to the origin along the filament direction (Oz). Interestingly, the qualitative shape and amplitude of these functions are very similar to what have been measured in gravitationally evolved simulations of the large-scale structure with a correlation bridge between the two peaks on both side (up and down) of the saddle point (at the origin of the frame), and exclusion zones in the perpendicular directions. In contrast, we also plot the $\mathcal{PF}$ cross-correlation for critical points of fixed heights (1 for filaments and 2 for peaks in this example) in Fig. A5. The exclusion zones in the transverse directions remain with the two peaks along the filament axis, but the correlation bridge between the peaks with the divergence at zero separation is replaced by an exclusion zone due to the different height constraint, which does not allow the peak and saddle (of different height) to stand too close to each other.

A4 BAO scale predictions

On BAO scales, expansion bias theory (e.g. Desjacques et al. 2018, and reference therein) allows us to anticipate the sign of the amplification on these scales. At leading order the peak two-point function is described by the first scale-dependent peak bias (Desjacques 2008; Desjacques et al. 2010):

$$\xi^{\rm (LO)}_{\mathcal{PP}} \approx \bar{b}_{10}(\nu_1)\bar{b}_{10}(\nu_2)\xi_{0,0} + \bar{b}_{01}(\nu_1)\bar{b}_{01}(\nu_2)\xi_{4,0} + [\bar{b}_{10}(\nu_1)\bar{b}_{01}(\nu_2) + \bar{b}_{01}(\nu_1)\bar{b}_{10}(\nu_2)]\xi_{2,0}, \quad \text{(A7)}$$

where the $\xi_{i,j}$ are defined as

$$\xi_{i,l} = \int \frac{{\rm d}^3k}{(2\pi)^3} P_{\rm s}(k) k^i j_l(kr), \quad \text{(A8)}$$

with j_l the spherical Bessel functions of order l, and the bias factors $\bar{b}_{ij}$ are given by

$$\bar{b}_{10}(\nu, x) = \frac{1}{\sigma_0}\frac{\nu - \gamma\bar{u}}{1-\gamma^2}, \quad \bar{b}_{01}(\nu, x) = \frac{1}{\sigma_2}\frac{\bar{u} - \gamma\nu}{1-\gamma^2}, \quad \text{(A9)}$$

with the mean peak curvature $\bar{u} = -\langle x_{11} + x_{22} + x_{33} | x = \nu\rangle$. In equation (A7), the $\xi_{0,0}$ term corresponds to the linear local bias that dominates for very high peak thresholds. This contribution that only comes from the peak height constraint (Bardeen et al. 1986; Desjacques 2008) is typically negative for underdense regions and positive for overdense regions scaling like $\sigma_0 b_{10}(\nu) \approx \nu - 3/\nu$ at high ν.[9] Since we can anticipate this sign for a given critical type and choice of abundance, and given that correlations involve the product of bias factors in equation (A7), all observed bumps and

[9]Note that an extension of the predicted linear bias to the quasi-linear regime was performed in Uhlemann et al. (2017).

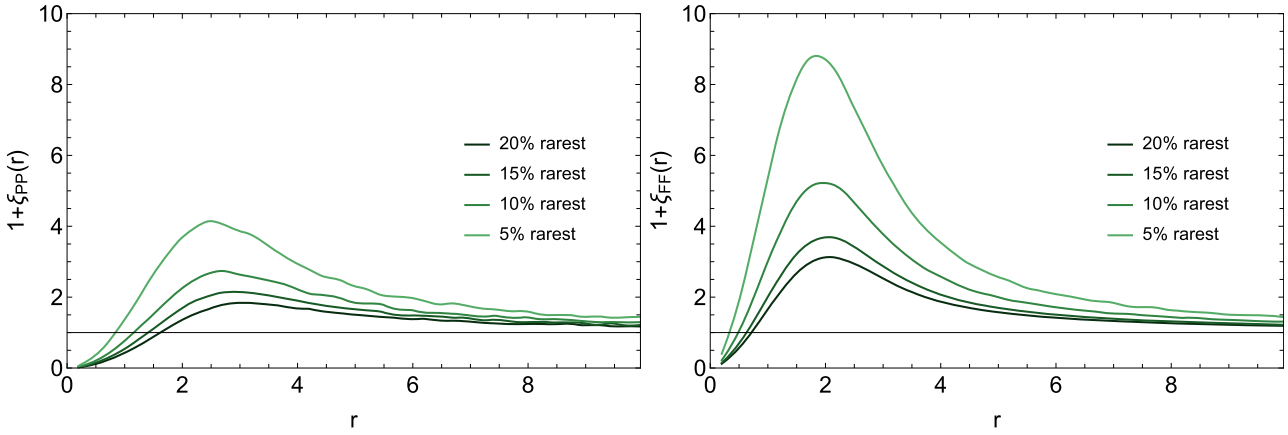

Figure A2. Auto 2pCFs (peaks on the left-hand panel, filaments on the right) for Gaussian random field with $n_s = -1.5$ and various abundances as labelled. The separation is in units of the smoothing length. The shape and amplitude of these functions match qualitatively the non-linearly evolved correlations presented in the main text (Fig. 2, top and middle left-hand panels). As expected the rarer the critical points, the larger the amplitude.

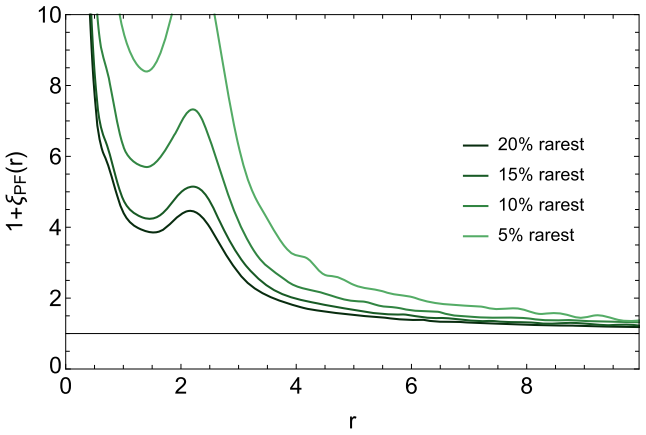

Figure A3. Peak–filament cross-correlations for Gaussian random field with $n_s = -1.5$ and various abundances as labelled. The separation is in units of the smoothing length. The shape and amplitude of these functions also match qualitatively their counterparts presented in the main text (Fig. 5, top left-hand panel).

dips in Figs 2–7 are qualitatively consistent with expansion bias theory. The contribution from the higher order derivatives, $\xi_{2,0}$ and $\xi_{4,0}$ typically tend to amplify and sharpen the BAO signature that tends to be damped by the smoothing operation, and it also reduces the inward shift of the BAO peak due to this smoothing (the BAO wiggles being asymmetric). However, the combined effect of those three terms occurs in some non-trivial manner depending on height, filter, and scale in particular. Note that higher order bias expansion have been performed (Desjacques 2013; Matsubara & Codis 2020) but are negligible to describe BAOs in Lagrangian space. Let us emphasize that the subsequent gravitational evolution will tend to broaden the initial sharp BAOs due to velocity drift. This effect can be investigated by modelling the Lagrangian displacement of initial peaks with perturbation theory (Desjacques et al. 2010) or more appropriately in our context using a Gram–Charlier expansion at the level of the joint statistics as was done on one-point statistics in e.g. Gay et al. (2012). This is left for future works.

A5 Cosmic crystal for Gaussian random field

The peak–filament, peak–wall, and peak–void correlation functions all present a maximum that we can use as a reference for the typical position of the first layer of, respectively, filaments, walls, and voids around a given peak. For Gaussian random field, we compute those correlation functions for the 15 per cent highest critical points and display the result in Fig. A6. The corresponding ratios are in agreement with those presented at redshift zero in the main text (Fig. 11).

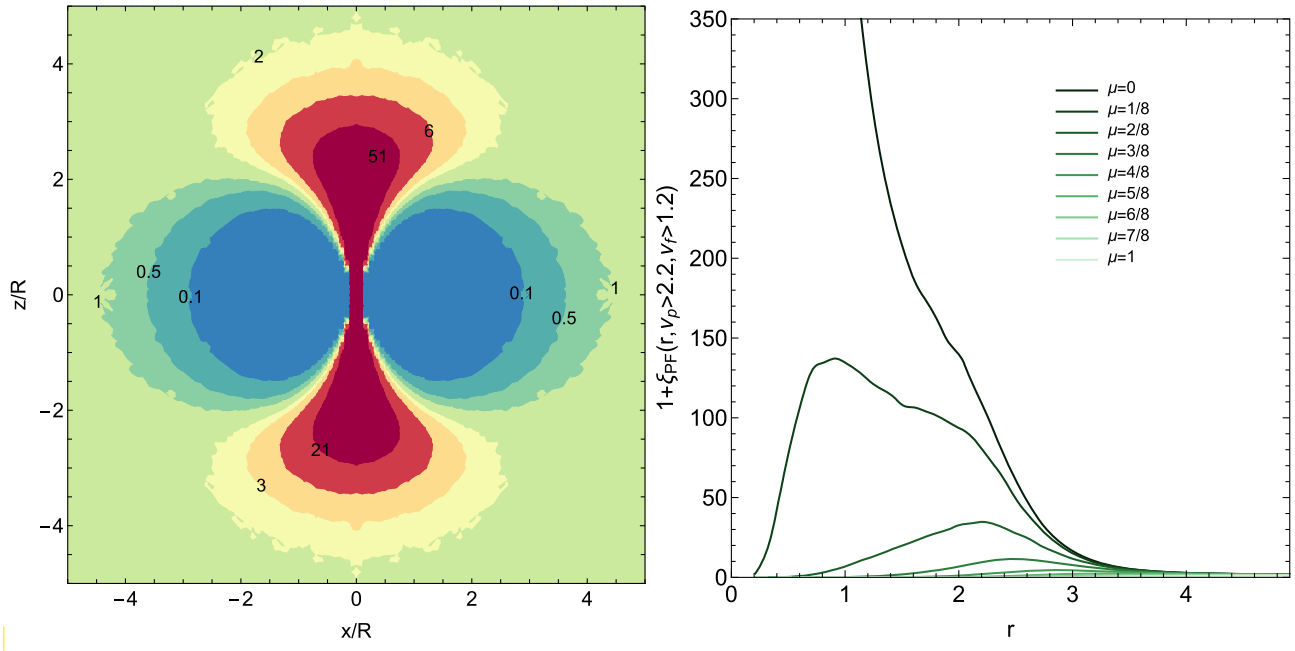

Figure A4. Left-hand panel: angle dependence of the peak–filament cross-correlation for Gaussian random field in the frame of a saddle for the 20 per cent rarest peaks and filaments. The origin is the location of the saddle point, (Ox) the direction of the void (largest negative curvature), and (Oz) the direction of the filament (positive curvature). This slice corresponds to $y = 0$. Right-hand panel: slices of the left-hand panel along different directions as labelled. Here μ is the cosine of the angle measured with respect to the x-axis. This figure can be compared favourably to redshift zero fields in the left-hand panel of Fig. 8 and the top left-hand panel of Fig. 9.

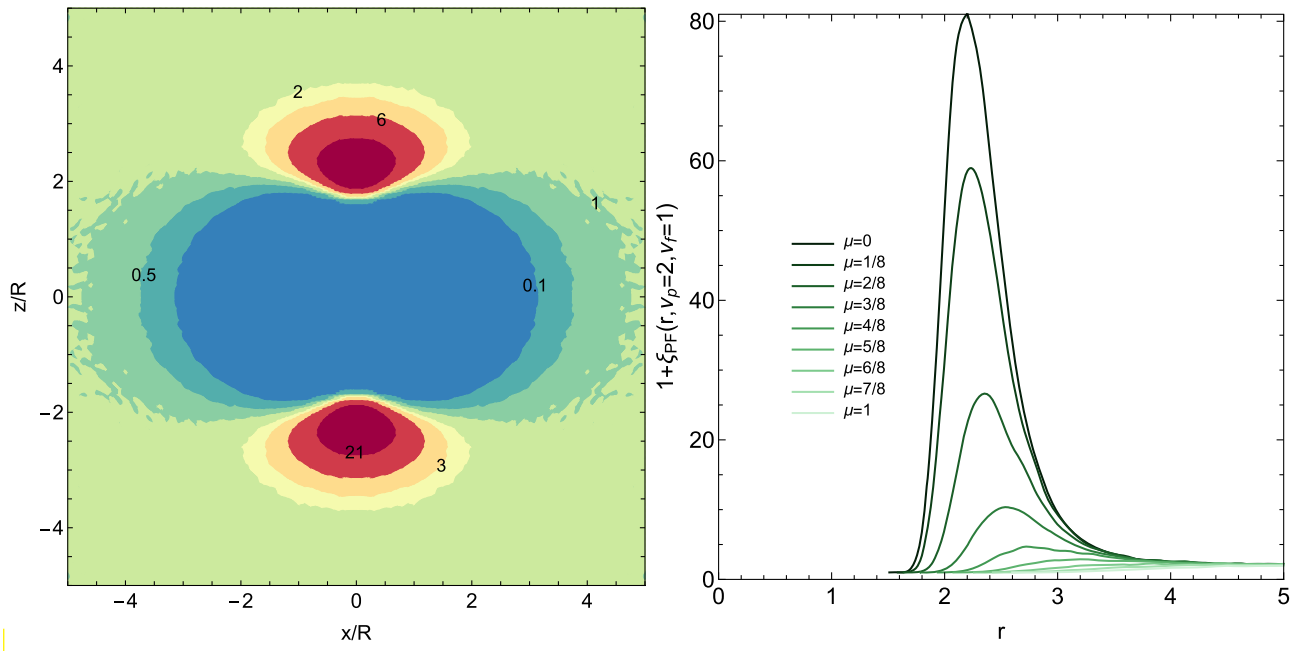

Figure A5. Left- and right-hand panels: same as Fig. A4 in the frame of a saddle of rarity $\nu_{\rm f} = 1$ when peaks are set to have a rarity $\nu_{\rm p} = 2$. Since the rarity does not overlap anymore, a global exclusion appears for all orientations, though the distribution of peaks remains strongly anisotropic.

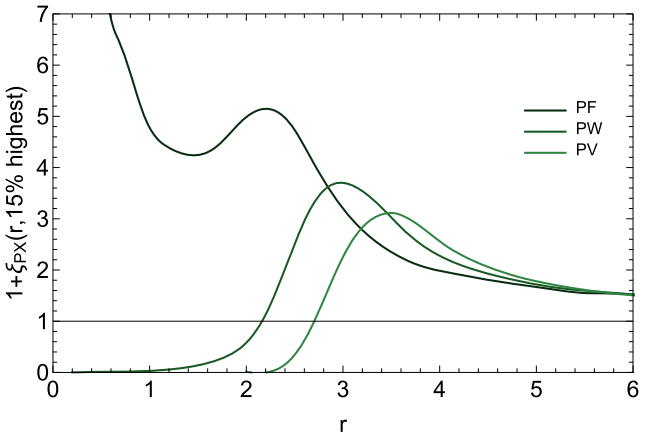

Figure A6. Cross-correlation between peaks and the 15 per cent highest critical points for a Gaussian random field with $n_s = -1.5$. The ratio of the radii at which these correlations reach their maxima is given by $r_{\mathcal{PF}}/r_{\mathcal{PW}} = 0.7 \approx 1/\sqrt{2}$ and $r_{\mathcal{PF}}/r_{\mathcal{PV}} = 0.6 \approx 1/\sqrt{3}$.

APPENDIX B: CROSS-CORRELATION DIVERGENCE

Let us finally address the origin of the difference in shape between correlations involving saddle points. In the main text, Fig. 5 displayed some divergence at this origin, whereas Fig. 4 did not. It turns out that the lack of divergence at the origin of $\mathcal{FW}$ correlation only reflects the rarity difference between the chosen filaments and walls. Indeed Fig. B1 now presents the $\mathcal{FW}$ correlation as a function of separation when the abundance above (in contrast to below as was used in the main text) a threshold rarity for wall points is varied from 20 per cent to 80 per cent, whereas that for filament points is fixed to 20 per cent. As expected, when the abundances are inconsistent, an exclusion zone occurs, whereas when they allow for some overlap, one recovers a divergence, as expected from critical event theory (Cadiou et al. 2020): filament and wall saddle points do get close to each other when a wall disappears. Note interestingly that these cross-correlations are quite insensitive to redshift evolution.

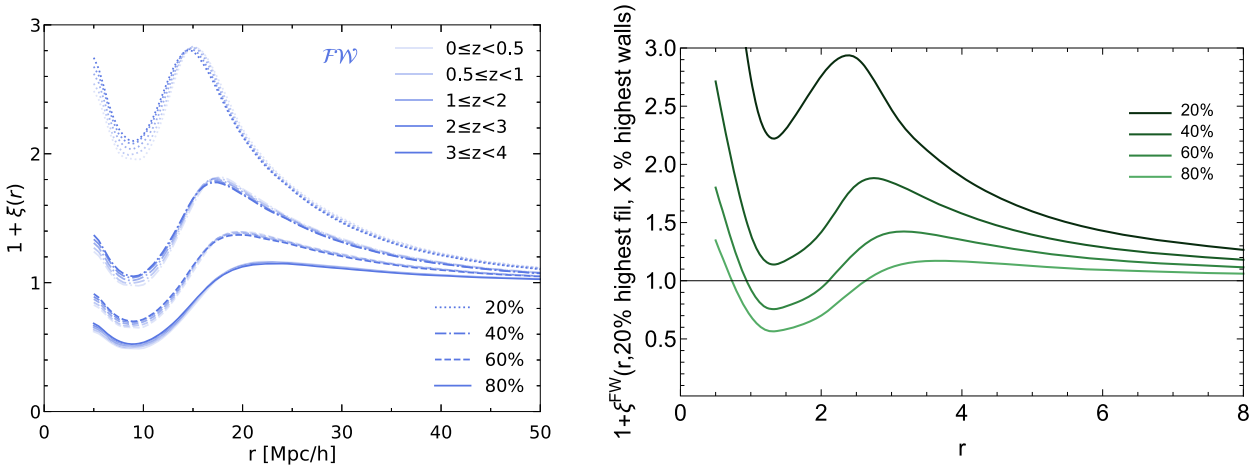

Figure B1. Left-hand panel: the behaviour of the $\mathcal{FW}$ correlation at small separation as a function of the abundance of wall points above a certain rarity threshold. For walls, it varies here between 20 per cent and 80 per cent, whereas filaments are fixed at 20 per cent. From the perspective of critical mergers (Cadiou et al. 2020), it is expected that filament and wall saddles merge during cosmic evolution, which was not seen in Figs 4 and 6. This was due to the chosen rarity difference between filaments and walls. As we increase here the rarity (including higher walls) the exclusion zone disappears and we recover the qualitative shape of the $\mathcal{PF}$ and $\mathcal{WW}$ correlations (Figs 5 and 7), including the divergence at small separation. Note also the stability of these correlations with redshift. Right-hand panel: same as left-hand panel for Gaussian random field. The separation is in units of the Gaussian smoothing length. The qualitative similarity between the left- and right-hand panels is striking.

This paper has been typeset from a TEX/LATEX file prepared by the author.